Geometry and subsidence history of the Dead Sea basin: A case for fluid-induced mid-crustal shear zone?

Uri S. ten Brink and Claudia H. Flores
U.S. Geological Survey, Woods Hole, MA 02543

Journal of Geophysical Research, Accepted 11/10/2011

Keywords: pull-apart basin, Retrograde metamorphism, muscovite, North Sea, basin subsidence, transform fault

Abstract:

Pull-apart basins are narrow zones of crustal extension bounded by strike-slip faults that can serve as analogs to the early stages of crustal rifting. We use seismic tomography, 2-D ray tracing, gravity modeling, and subsidence analysis to study crustal extension of the Dead Sea basin (DSB), a large and long-lived pull-apart basin along the Dead Sea transform (DST). The basin gradually shallows southward for 50 km from the only significant transverse normal fault. Stratigraphic relationships there indicate basin elongation with time. The basin is deepest (8-8.5 km) and widest (~15 km) under the Lisan about 40 km north of the transverse fault. Farther north, basin depth is ambiguous, but is 3 km deep immediately north of the lake. The underlying pre-basin sedimentary layer thickens gradually from 2-3 km under the southern edge of the DSB to 3-4 km under the northern end of the lake and 5-6 km farther north. Crystalline basement is ~11 km deep under the deepest part of the basin. The upper crust under the basin has lower *P* wave velocity than in the surrounding regions, which is interpreted to reflect elevated pore fluids there. Within data resolution, the lower crust below ~18 km and the Moho are not affected by basin development. The subsidence rate was several hundreds of m/m.y. since the development of the DST ~17 Ma, similar to other basins along the DST, but subsidence rate has accelerated by an order of magnitude during the Pleistocene, which allowed the accumulation of 4 km of sediment. We propose that the rapid subsidence and perhaps elongation of the DSB are due to the development of inter-connected mid-crustal ductile shear zones caused by alteration of

feldspar to muscovite in the presence of pore fluids. This alteration resulted in a significant strength decrease and viscous creep. We propose a similar cause to the enigmatic rapid subsidence of the North Sea at the onset the North Atlantic mantle plume. Thus, we propose that aqueous fluid flux into a slowly extending continental crust can cause rapid basin subsidence that may be erroneously interpreted as an increased rate of tectonic activity.

1 Introduction:

Pull-apart basins, which form by crustal extension parallel to their long axis, provide a window into the deformation of the continental crust. Such basins are bounded by two strike-slip fault strands along their long axis and by one or two diagonal normal faults that connect between the strike-slip fault strands (e.g., [*Aydin and Nur*, 1982; *Crowell*, 1974; *Garfunkel and Ben-Avraham*, 1996]) or are located along a jog in the strike-slip fault (e.g., [*May et al.*, 1993]; [*Seeber et al.*, 2006]). Their shape is often rhombic or that of a parallelogram. The depth to the bottom of the extended block and the subsidence rate of the basin are undefined in this kinematic description. One option is for the strike-slip fault strands to curve with depth and merge to a single fault in the middle crust (e.g., [*Segall and Pollard*, 1980]. Another option is for the separate strike-slip fault strands to extend into the upper mantle, in which case, the Moho is down-dropped [*Ben-Avraham and Schubert*, 2006]. A third alternative is for the strike-slip faults to terminate against or curve into a mid-crustal detachment (e.g., [*Arbenz*, 1984; *May et al.*, 1993; *Seeber et al.*, 2006]).

Sandbox models, ([*Wu et al.*, 2009] and references within), and elastic boundary-element models driven by motion from below [*Katzman et al.*, 1995; *ten Brink et al.*, 1996] have attempted to recreate the 3-D geometry of pull-apart basins. Finite-element thermo-mechanical models using extrapolated laboratory measurements of rock rheology to lithospheric strength [*Petrunin and Sobolev*, 2006; *Petrunin and Sobolev*, 2008] have also modeled the subsidence rate and history of these basins. Recent advances in the study of continental extension focused on the role of strain localization and dynamic strength evolution, particularly in the middle crust [*Lavier and Manatschal*, 2006; *Regenauer-Lieb et al.*, 2008]. These models have not yet been applied to pull-apart basins.

Here we present observations which suggest a significantly weaker middle crust under the Dead Sea pull-apart basin (DSB) than would be predicted by standard rheological models. The basin (Figure 1) overlies continental crust with a relatively simple thermo-mechanical history. The continental crust of the eastern Mediterranean margin is a Triassic-Jurassic passive continental margin with minor later tectonic activity [*Freund et al.*, 1970; *Garfunkel*, 1997]. Heat flow in this region is low (45-54 mW/m^2; [*Eckstein and Simmons*, 1978; *Galanis et al.*, 1986]) and the narrow dimension of the basin (~10 km) assures that elevated heat flow as a result of extension dissipates rapidly in the surrounding crust [Pitman and Andrews, 1985; *ten Brink et al.*, 1993]. Hence, crustal extension of the DSB represents extension of the rheologically-stratified crust without the complications of a mantle heat source.

The DSB is a long (~150 km), narrow (≤15 km), and deep (< 8.5 km) basin along the Dead Sea continental transform (DST). Interpretation of the gravity field over the basin [*ten Brink et al.*, 1993], later confirmed by seismic refraction profiles [*Mechie et al.*, 2009; *ten Brink et al.*, 2006], indicates that within data resolution (2-3 km), The Moho is not deflected upward under the basin. Seismic refraction profiles also show the 18-km-deep upper-to-lower crust boundary not to be deflected upward or downward [*Mechie et al.*, 2009; *ten Brink et al.*, 2006]. The absence of appreciable deflection at the mid-crust and Moho levels suggests that, despite its large depth, basin deformation and crustal extension are confined to the upper crust.

The DST is a strike-slip fault system (Inset in Figure 1), which currently accommodates 5±1.5 mm/yr of left-lateral motion between the Arabian and African tectonic plates [*Le Beon et al.*, 2008]. A total offset of 105-110 km has accumulated along the plate boundary since the middle Miocene (~17-18 Ma) [*Freund et al.*, 1970; *Quennell*, 1958]. The Dead Sea Basin has been accumulating sediments since the formation of the plate boundary (e.g., [*Calvo and Bartov*, 2001] and continues to subside at present as evidenced by its low surface elevation (422 m below sea level).

In this paper we analyze the structure and subsidence rate of the DSB to further constrain models of crustal extension in cold continental crust. The paper combines the results of 2-D ray tracing models of seismic refraction data, with 3-D seismic tomography of explosions, mining shots and earthquakes, and 2.5-D gravity modeling in the vicinity of the Dead Sea Basin to better constrain the 3-D structure of the basin and its surrounding. Simple back-stripping analysis of the basin fill helps elucidate the recent change in subsidence rate. The 3-D structure of the basin and its varying subsidence rate with time are discussed in the context of ductile shear bands that might develop in the middle crust. Ductile shear bands might develop as feldspar undergoes retrograde metamorphism to white mica in the presence of aqueous fluids.

2 Data analysis

2.1 Wide Angle reflection and refraction

Seismic data were collected during a multinational seismic refraction experiment on October 21-22, 2004 [*ten Brink et al.*, 2006]. 753 miniature seismic recorders (RefTek 125, nicknamed Texans) were deployed along a 280-km-long North-South profile along the transform valley and a 250-km-long East-West profile across the deep part of the basin a few km north of Amazyahu Fault (Figure 1). The Texans were attached to a single vertical 4.5 Hz geophone, and were placed at intervals of 0.65 to 0.75 km along the profiles. Nine controlled explosions, eight of 1000 kg dynamite each and one of 3000 kg (Table 1), were detonated at the bottom of 25-40-m deep boreholes along the receiver lines. Two additional explosions, 750-kg dynamite each, (Table 1; Figure 1) were suspended at a depth of 50 m within the waters of the Dead Sea.

Prior to analysis the seismic records from all the receivers were filtered with an Ormsby bandpass filter with corner frequencies at 1-2 and 10-20 Hz. The records were arranged as common-shot gathers and plotted in reduced travel-time format according to their shot-receiver offset (Figure A1). Phase arrivals, corresponding to refractions and prominent reflections were picked. The picking error is estimated to be +/- 100 ms. Shot and receiver locations were projected onto a best-fit straight line for each of the respective north-south and east-west profiles to allow 2-D analysis. A forward and inverse ray tracing routine [*Zelt and Smith*, 1992] was used to model interactively [*Song and ten Brink*, 2004] the 5853 phase arrivals for the E-W line

(Figure 2) and the 2532 phase arrivals for the N-S line, and to generate a 2-D velocity model along each profile. Modeling results of the east-west line were published by *ten Brink et al.* [2006]

The structure along the E-W profile is relatively 2-D, and reciprocal travel-time arrivals can be identified to large shot-receiver offsets. Therefore, crustal structure along the E-W profile could be modeled down to the Moho (Figure 3). As detailed in *ten Brink et al.* [*2006*], structures with amplitudes of less than 2.5 km in the sampled Moho or the edges of the profile are not resolvable. Modeling the North-South line as a 2-D structure was difficult in the area of the Dead Sea Basin between shots 4 and 6, because the shot-receiver geometry does not provide reciprocity due to the location of the shots within the lake and many of the receivers along its eastern shore (Figure A2). The regions between shots 1 to 4 and shots 6 to 7 are modeled to an approximate depth of 15 km. Deeper arrivals could not be modeled along the N-S profile because the basin is narrow and ray paths probably run partially or completely within the surrounding crust.

2.2 Travel-time tomography

In addition to the controlled explosions, the seismometers also recorded ten mining explosions and one shallow (~15 km) local earthquake (Figure 1, Table 1) during multiple recording windows of 20 minutes during October 21-22, 2004. First arrivals for all sources were picked in unreduced time format because the locations of mining explosions were initially unknown (Figure 4, Figure A3). A few first-arrival data, recorded by seismometers of the Geophysical Institute of Israel seismic network were also picked. The seismic records from the Texans were filtered as before. For consistency, the explosion data from the seismic experiment was also re-picked in this manner. A total of 12,961 arrivals were picked for the tomography study; 6449 arrivals from the explosion shot data and 6512 arrivals from the other events. Data generated by the controlled explosions were assigned a picking error of +/- 250 ms and other data (mine explosion or earthquakes) were assigned a picking error of +/- 300 ms. Events not listed on the Israeli earthquake catalogue were identified by seismic arrivals from our receivers in the Lisan Peninsula in the Dead Sea Basin. Receivers located in the Lisan Peninsula consistently detected

clear first arrivals from very small events, even when the rest of our deployed receivers detected very weak or no arrivals. Arrivals detected but not related to the experiment shot data were preliminarily located using HypoInverse 2000 [*Klein*, 2002] with a simple 1-D velocity model [*Al-Tarazi et al.*, 2006]. Since most of the extra events were assumed to be from quarry explosions, a general new location was identified using imagery in Google Earth© and known locations of quarries [*Abu-Ajamieh et al.*, 1988] in the vicinity of the initial location provided by HypoInverse. In most cases the new location at an established quarry was easily found due to the proximity of the preliminary location and the quarry. An approximate location error of +/- 2 km was assigned, which translated to change in RMS of ~0.1 s in the HypoInverse program. However, the tomographic coverage is mainly the result of the sparse shot spacing and the concentration of hundreds of receivers along two lines instead of being evenly distributed in space (Figure 5a, Figure A4).

We used the 3-D first arrival regularized inversion method of [*Zelt and Barton*, 1998] that relies on a linearized iterative approach to search for the simplest velocity model that will fit the observed first arrivals within the accuracy of the picked error. The velocity model and ray paths are both updated during each iteration with the goal of minimizing the normalized misfit χ^2 while keeping the velocity model smooth. Weight parameters in the inversion were varied with depth with the least weight in the near-surface part of the model and increasing weight with depth. An accepted final model has a low χ^2 value and RMS values between 600 – 500 ms. Below χ^2 values of 4, successive iterations of the inversion do not show significant improvement in RMS and the small scale variability of the velocity model increases.

The velocity model volume consisted of 351x401x56 nodes in the x, y and z directions with one km spacing for a total of 140,807 nodes. Locations of events and stations were transformed from latitude and longitude locations into UTM coordinates. These UTM coordinates were then translated into model x, y, and z locations in units of kilometers. We used a reference point of 30.9860°N 35.3633°E (UTM coordinates 36R, 725678.1907, 3430447.4068) as the center point of the model (x=175, y=200) and model limits of x= 0, 350, y= 0, 400, and z=-5, 50 km. A 2 minutes (3.25 km) interval topography grid was re-sampled and transformed into a 1 km interval

topography grid. This surface grid cuts into the background velocity volume to restrict ray path propagations to only below the topography.

As discussed in *Zelt and Barton* [*1998*], the inversion grid used to calculate the slowness of the ray paths can have a larger grid size than that of the velocity model. To calculate the final velocity model we started with a large inversion cell size (25 km x 25 km x 5 km) and gradually reduced the size (minimum of 10 km x 10 km x 1 km; Table 2). With a large grid size, smoothed general velocity trends can be approximated and found quickly. Reduction in inversion grid size with each iteration step was used to fine-tune the absolute velocities in the model [*Haberland et al.*, 2007] and improve model fit (Table 2). Resolution tests of the model are discussed in the appendix.

Starting with a laterally homogenous velocity model (after [*Al-Tarazi et al., 2006*]), and the largest grid size, the major features of the velocity model can already be identified such as the low velocity regions of the DSB and the Timna-Gharandal region. Differences in crustal velocity with depth appear across the DST particularly along the E-W profile. Several other starting models with velocity variations between the two sides of the transform valley were also tested. Although the goodness of fit of the starting homogenous model is slightly worse than the starting models with lateral variations across the transform valley, the final model is as good or better than the heterogeneous starting models (Table A1). All final models regardless of the starting model consistently show low and high velocities in the same areas and depths.

Plots of ray coverage (Figure 5a, Figure A4) help identify those parts of the model, which are well resolved. Ray coverage is determined by the geometry of the receivers and sound sources. The plots are binned at source-receiver intervals of 20 km. Using a basic rule of thumb of one quarter of the source-receiver distance as the approximate depth of the turning point of a ray path, we note that the top 5 km of the model is well covered along the receiver lines. Model depth of 5-20 km is sampled by distributed ray coverage between the two receiver lines, and the coverage of model depths >20 km is sparse.

Checkerboard tests (see supplementary material) show that only large-scale features in the velocity model can be resolved (Figure 5b) due to the geometry of the shot and receivers. In addition to the areas along the receiver lines in the model, the resolution of the checkerboard is best at the top 2-5 km of the model, where velocity contrasts in the final model are large (±15%) and it decreases with depth, where the velocity contrast is smaller (9-7%). Low velocity areas are difficult to resolve in general in tomography of first-arrival travel time, due to the tendency of the first arrivals to travel through the faster regions of the medium. The resolution of the model seems to be robust enough in the upper 12 km of the model, which is the model region needed to determine the general shape of the Dead Sea basin.

2.3 Gravity:

Gravity profiles were extracted from the combined database of gravity measurements of Israel and Jordan [*ten Brink et al.*, 1999]. The two profiles were sampled at 1 km spacing along the E-W and N-S profiles. Free-air gravity data was modeled with GM-SYS™ software to derive density models along the two profiles (Figures 6a, 6b, and 7). Two different strategies were used in each profile. To test the velocity model along the east-west profile, we converted the *P* wave velocity model of *ten Brink et al.* [*2006*] to a density model using *P* wave velocity to density relationship [*Brocher*, 2005] and compared the calculated gravity from this model to the observed gravity profile (Figure 6a top). The calculated gravity shows a good fit to the observed gravity profile in the middle section but not at the edges of the profile, possibly because the velocity model is not as well constrained at the western edge of the model, and out-of-plane density effects in Al-Jafr Basin dominate the eastern edge of the model.

Results from extensive geophysical work in the transform valley and the surrounding highlands were used to build a density model along the north-south profile (Figure 6b, 7). This work includes general crustal studies of the Middle East for depths to the crystalline basement and upper sedimentary layers [*Rybakov and Segev*, 2004; *Segev et al.*, 2006], gravity and airborne magnetic studies [*ten Brink et al.*, 1999; *ten Brink et al.*, 2007], density-depth profiles from well log data [*Rybakov et al.*, 1999], sediment thickness beneath the western and eastern and western highlands from boreholes [*Abu Saad and Andrews*, 1993; *Garfunkel and Derin*, 1984; *Gilboa et*

al., 1993], and basin geometry from seismic reflection studies [*Al-Zoubi and ten Brink*, 2001; *Al-Zoubi and ten Brink*, 2002; *Al-Zoubi et al.*, 2007; *Ginzburg et al.*, 2007; *Lazar et al.*, 2006]. Because of the lack of reliable crustal velocities along the N-S line, we used the velocity-derived crustal densities beneath and outside the basin along the E-W (Figure 6a) for the crust beneath the basin and outside the basin along the N-S profile. Unlike the E-W profile, the N-S profile uses the 2 1/2 dimensional modeling to account for gravitational attraction of the rocks outside the narrow basins and for other potential out-of-plane bodies that may contribute to the total gravity profile. The basin width is loosely modeled from the observed surface expression and at the deeper part of the basin it is inferred to narrow with depth following seismic reflection profiles [*Al-Zoubi and ten Brink*, 2001; *Kashai and Croker*, 1987; *ten Brink and Ben-Avraham*, 1989]. The gravity model along this profile is used to augment our interpretation of the structure of the basin.

3. Interpretation:

3.1 Shape of the Basin

Previous studies were able to map the depth of the Dead Sea basin fill in several locations. The most direct evidence is the Sedom Deep-1 borehole (Figure 6a), which reached a depth of 6445 m below the surface (6830 m b.s.l), and sampled the entire basin fill of continental and lacustrine mid-Miocene-to-present sediments, including a 900 m thick layer of Pliocene salt [*Gardosh et al.*, 1997]. Identification of the base of the basin fill on seismic reflection profiles is more difficult. Continental and lacustrine sediments of the Hazeva Group fill the bottom of the Dead Sea basin. From geological studies the lower two formations of the Hazeva Group with a maximum thickness of 200 m, were deposited before the Dead Sea Transform and the Dead Sea basin started their activity [*Calvo and Bartov*, 2001]. Hence, the uncertainty in locating the base of basin fill is ~200 m. South of Amazyahu Fault, *Al-Zoubi and ten Brink* [2002] identified the base of the basin fill in a seismic reflection line, as dipping northward for 35 km from the southern end of the basin to a depth of ~5 km (Figure 6b). Pre-stack depth migration of seismic reflection profiles between Amazyahu fault and the Lisan Peninsula (Figure 6b) maps the base of the basin at a depth of ~7 km [*Ginzburg et al.,* 2007] with an estimated uncertainty of ±200 m (M. Reshef, pers. Comm., 2008). The frequency of micro-earthquakes in the central basin

(between km 150-200 in Figure 6b) increases five fold below a depth of 7-8 [Braeuer et al., submitted], and we interpret this depth to mark the boundary between semi-consolidated basin fill and the consolidated pre-basin Paleozoic to Early Cenozoic sediments. Our E-W seismic refraction profile, which crosses the basin a few km north of Amazyahu fault, placed the base of the basin at 6.6 km depth b.s.l., (Figure 6a; [*ten Brink et al.,* 2006]). Using poor-quality seismic reflection data beneath the Lisan Peninsula, *Al-Zoubi and ten Brink* [2001] identified the base of basin fill under the Lisan Peninsula at ~8 km and suggested that most of the fill there consists of salt. *Mechie et al.* [2009] placed the base of basin fill under the Lisan Peninsula at 8.5 km (Figure 6b). Only one refraction study was previously conducted in the northern part of the basin [*Ginzburg and Ben-Avraham*, 1997]. It modeled an interface with velocity contrast of 4.8 to 6 km/s dipping from 6 km depth at the northern edge of the lake to 8 km at the Lisan peninsula (Figure 6b). This interface was interpreted, however, as the bottom of the pre-basin sediments below the basin fill, not the base of the basin fill itself. The base of basin fill in seismic reflection data north of the lake is poorly defined [*Al-Zoubi et al.,* 2007; *Lazar et al.,* 2006; *Shamir et al.,* 2005] probably because of the narrow width of the basin. *Lazar et al.* [2006] proposed a transverse fault (Kalia fault) buried under young sediments located about 15 km south of the northern shore of the lake, which coincides with the epicenter of the M 5.1 2004 earthquake. We use the depth constraints from the aforementioned seismic reflection and refraction studies (except for that of *Ginzburg and Ben-Avraham* [1997]) in the gravity models (Figures 6a and 6b) and densities from the down-hole density profile of Sedom Deep-1 borehole [*Rybakov et al.,* 1999].

A sediment velocity gradient of 2.4 - 4.9 km/s is derived from ray tracing along the E-W line ([*ten Brink et al.,* 2006]; Figure 6a), and is comparable with sonic log velocity gradient from Sedom Deep-1 borehole (Inset in Figure 6a). It increases from 4.9 km/s to 5.3 km/s at the base of the fill. *Mechie et al.* [2009] identified a uniformly high basin fill velocity of 4 km/s at the surface increasing to 4.8 km/s at the base, which probably reflects the existence of salt in most of the depth section under the Lisan Peninsula. Sediment velocity within the basin in our tomographic model is higher (4.2-5.4 km/s below ~ 1 km depth, Figure 6b) than in the sonic logs and the E-W ray-tracing model but is lower than in the ray-tracing model under the adjacent

highlands (Figures 6 and 8). The coarse resolution of the tomographic model and the uneven distribution of shots and receivers tend to average the velocity across the sharp lateral boundary between the slow velocities within the basin and the high velocities in the surrounding regions (Figure 6a). We chose the 5.4 km/s velocity contour as the base of basin-fill in the tomographic model because it fits well with depth determinations from the borehole, seismic reflection profiles, and the 2-D ray-tracing model along the E-W profile. Using the 5.4 km/s contour in the tomography model as the base of the basin fill, we make a general map of the shape of the basin (Figure 8a). The deepest part of the basin is located under the Lisan Peninsula at a depth >8 km. The basin is asymmetric along axis, as already noted in gravity modeling [*ten Brink et al.,* 1993], extending 50-60 km to the north and 80-100 km to the south.

The northern part of the basin, which is located under the lake, continues to be unusually deep (>6 km) in the tomographic results (Figure 6b, 8a), but shallows rapidly at or north of the northern shore of the lake. Gravity modeling suggests a more gradual thinning toward the northern end of the basin (Figure 6b). In an attempt to reconcile the gravity model in the northern basin with the tomographic results, we increased the basin-fill density there by placing a 1-km thick dense layer (2650 kg/m^3) within the basin fill. This dense layer may represent basalt flows extending from Zarqa' Ma'in on the eastern shore of the lake. However, even with the increased density of the basin fill, the modeled basin floor from gravity at the north end of the basin cannot resemble that from the tomography. On the other hand, tomographic models tend to focus lower velocities beneath the sparse explosions to improve fit to the data, and the low-velocity under shot 6 (km 235 in Figure 6b) is therefore interpreted as an artifact.

A 2-D ray-tracing model, which uses reciprocal phases between Shots #6 and #7 north of the Dead Sea, indicates that basin thickness decreases gradually for 28 km north of the lake and then decreases rapidly in the vicinity of Ghor Katar (Figure 9a). A small exposure of older basin fill rocks (Pleistocene Samra Formation) and a young volcanic outcrop are located near Ghor Katar [*Begin*, 1975; *Bender*, 1974]. This exposure is coincident with a positive peak in the gradually increasing Bouguer [*ten Brink et al.,* 1999] and free-air (Figure 6b) gravity fields.

To the south, the tomography results and gravity model show that the basin remains relatively deep (6-7 km) until Amazyahu Fault [Figure 6b, *Al-Zoubi and ten Brink,* 2001; *Ginzburg et al.,* 2007]. The basin floor rises to a depth <4 km along the Amazyahu normal fault [*Ginzburg et al.,* 2007], but is deeper again south of Amazyahu Fault (4-5 km, [*Gardosh et al.,* 1997; *Ginzburg et al.,* 2007], Figure 6b). The basin shallows southward gradually and disappears about 50 km south of Amazyahu Fault [*Al-Zoubi and ten Brink*, 2002, Figure 7].

Basement reaches close to the surface south of the DSB as reflected in the high seismic velocities close to the surface (Figure 6b, Figure 9b). This area is also up to 200 m above sea level. Two small basins were identified at the southern end of our study area in previous gravity [*ten Brink et al.,* 1998], seismic [*Frieslander*, 2000], and aeromagnetic studies [*ten Brink et al.,* 2007]. The Gharandal basin immediately south of the basement high of the central Arava valley is approximately 2 km wide, 17 km long, and no more than 500 m deep. Its size is too small to be detected by the tomography method but it shows in the 2-D ray-tracing model as a region of slow seismic velocities (2.4 km/s) near the surface (Figure 9b). Timna basin at the southern end of our model is approximately 6 km wide, 30 km long and 1-1.5 km deep [*ten Brink et al.,* 1999]. Due to its larger size, the Timna basin is sampled in the tomography and the wide-angle with seismic velocity of 3.4 km/s, but because it is located at the edge of the seismic model, the shape and depth and width of this basin are smeared (Figure 6b, Figure 9b). The gravity profile shows a relatively negative anomaly over the Timna basin (Figures 6b, 8).

3.2 Thickness of older sediments

The region surrounding the DST in Israel and Jordan is covered by sedimentary rocks of variable thickness and composition ranging in age from the latest Pre-Cambrian to the Eocene [*Garfunkel and Derin, 1984*]. Pre-Permian Paleozoic sandstones increase in thickness to the south and east away from the Levant Triassic-Jurassic passive continental margin, whereas Mesozoic and Cenozoic sedimentary thickness increases to the north and east [*Bender*, 1974; *Garfunkel and Derin, 1984*]. Limestone, dolomite, and chalk were deposited on the ancient continental shelf and fluvial sediments consisting mainly of sandstone were deposited landward of the shelf [*Garfunkel and Derin, 1984*]. The ancient coastline, which was the boundary between the two

lithological domains, changes its orientation from N-S to E-W at about the latitude of the DSB. As a result the DST south of the DSB is underlain by thin mostly sandstone or is devoid of sediments, and the DST north of the DSB is underlain mostly by much thicker carbonate rocks [*Garfunkel and Derin, 1984*; *Andrews*, 1991, 1992a, 1992b; *Segev et al.,* 2006]. Specifically, the total thickness of the older sedimentary section on the western flank of the DST increases from <1 km at the southern end of our study area to > 6 km at the northern end [*Garfunkel and Derin, 1984*; *Segev et al.,* 2006]. However, the exact thickness variations and the location of the lithological boundary beneath the DSB itself are unknown.

Wide-angle seismic reflection profiles across the basin place the contact between the older sediments and the underlying crystalline basement at *P* wave velocity of 5.9 km/s, and at a depth of 10-11 km north of Amazyahu Fault (Figure 6a, [*ten Brink et al.,* 2006]) and under the Lisan Peninsula [*Mechie et al.,* 2009]. The tomographic inversion shows an increased velocity gradient at 5.8 km/s, which we interpret to be the top of the crystalline basement. The depth to the 5.8 km/s contour varies from 12 km under the Lisan Peninsula and the southern part of the lake to 7 km under the Amazyahu Fault and 9-10 km under the northern end of the lake (Figure 8b). The difference between the depth of basin fill (Figure 8a) and the depth to the crystalline basement (Figure 8b) represents the thickness of the older pre-basin sediments. The older sediments increase in thickness from 3 km in the southern half of the basin to 4 km under the Lisan peninsula and under the lake to 5-6 km under the Jordan valley north of the Dead Sea. However, the lateral resolution of this change is probably no better than 20-25 km as evident by the extension of basin contours beyond the width of the basin (Figure 8b).

The 2 1/2-D gravity model along the axis of the DST is compatible with the thickness variations in the tomography model (Figure 7b). The model accounts for variations in the width of the basin along the axis of the DST, and known changes in the thickness and lithology of the sediment cover immediately west and east of the DST valley. The gravity model under the DST assumes that the south-to-north variations in the thickness and lithology of the older sediment layer is similar to that under the western flank of the DST (Figure 7), implying that the general plate boundary at depth is closer to the eastern side of the transform valley. The calculated

gravity from this model produces a good fit to the observed gravity (Figure 6b, top). Note that the northward increase in thickness of the older pre-basin sedimentary layer is not manifested in the gravity field. This is due to the change from mainly sandstone composition in the south, which has an average density of 2550 kg/m^3 to limestone and dolomite, which have an average density of 2650 kg/ m^3 [Rybakov et al., 1999].

3.3 Deeper structure:

E-W profiles from ray tracing of wide-angle reflection data show an anomalously low seismic velocity in the upper crust below the DSB (6.1-6.5 km/s, [*ten Brink et al.,* 2006], Figure 6a; 5.9-6.4 km/s, [*Mechie et al.,* 2009]) relative to upper crustal velocity in the surrounding area (6.3-6.5 km/s). Whether the lower P-wave velocity in the upper crust is associated with a lower density cannot be resolved. Models with lower density following empirical velocity-density relationships [*Brocher et al.,* 2005], and models without a density anomaly in the upper crust fit both the N-S and E-W gravity profiles equally well. Because we do not know of processes capable of reducing upper crust density under the basin, we do not assign anomalous density to the region of anomalous velocity.

The lower crust velocity under the DSB in the E-W wide-angle seismic profiles (6.8-7 km/s; Figure 6a) is similar to that to the east and west, giving no indication of lower crustal extension, contrary to predictions from thermo-mechanical models with layered crustal rheology [*Petrunin and Sobolev,* 2006, 2008). The upper-to-lower crustal boundary under the basin at depth of 18 [*ten Brink et al.,* 2006] to 20 km [*Mechie et al.,* 2009] is not deflected upward as predicted by analog models of brittle upper crust and ductile lower crust [*Wu et al.,* 2009]. Micro-seismic activity in the region between Amazyahu Fault and the Lisan decreases five-fold below a depth of 17 km ([*Braeuer et al.,* submitted], Figure 6b). The Moho is at depth of 30-31 [*ten Brink et al.,* 2006] to 32.5 km [*Mechie et al.,* 2009]. The wide-angle seismic data ([*Ginzburg et al.,* 1979; *ten Brink et al.,* 2006], Figure 6a) and the gravity model (Figure 7a) suggest that crustal thickness decreases across the passive continental margin toward the Eastern Mediterranean Sea.

4. Basin subsidence

Changes in subsidence rate with time provide an important constraint on the formation process of pull-apart basins. Subsidence rate is commonly estimated using the backstripping method [*Steckler and Watts,* 1978], which successively de-compacts the present-day stratigraphic thickness of layers within the basin to their thickness at the time of deposition. Corrections for water depth at the time of deposition and for variations in sea level from present sea level must also be made. Thus, the Airy compensated tectonic subsidence, Y, is

(1)
$$Y = W_d + S^* \left[\frac{(\rho_m - \overline{\rho}_s)}{(\rho_m - \rho_w)} \right] - \Delta_{sl} \frac{\rho_m}{(\rho_m - \rho_w)}$$

Where W_i is the water depth, S^* is the de-compacted sediment thickness, Δ_{sl} is the height of mean sea level with respect to a reference surface and ρ is the density for the mantle (m), sediment layer (s) and water (w) respectively. For the Dead Sea basin, which was disconnected from the world oceans for much of its history and contains fluvial and lacustrine sediments, sea level and water depth are set to zero. The backstripping equation is further simplified by ignoring isostatic compensation. Isostatic compensation can be ignored because the basin is narrow (10-15 km) relative to typical flexural wavelengths of the lithosphere [*ten Brink et al.,* 1993]. Hence, $Y = S^*$. The de-compacted sediment thickness is,

(2)
$$S^* = \left(\frac{1 - \varphi_{si}}{1 - \varphi^*_{si}} \right) S$$

Where, S the layer thickness after compaction for a given depth, φ_{si} is the layer porosity after it underwent compaction for a given rock type at a specific depth and φ^*_{si} is the initial layer porosity before compaction. Variations of porosity with depth of burial can be complex, but are often simplified by an exponential decrease with depth

(3)
$$\varphi_{si} = \varphi^*_{si} e^{-cz}$$

Where φ_{si} is the porosity for a formation at a specified depth, φ^*_{si} the initial porosity at the surface, c is the lithology dependent coefficient rate of exponential decrease in porosity with depth and z is a given depth [e.g., *Hölzel et al.,* 2008]. Formation porosities are calculated using values for φ^*_{si} and c is given by *Holzel et al.* [2008 (Table 3)

449 The Sedom Deep-1 well is located close to the deepest part of the basin (Figure 1) and is
450 therefore considered to be a representative sample for the total basin subsidence history. We
451 used the approximate percent compositions of marls and sandy marls in the Sedom Deep-1 well
452 log to calculate φ and c for the different layers of basin fill (see Table 3). The well section was
453 divided based on the interpretation of the gamma-ray log to six major depositional sections
454 [*Larsen et al.,* 2002]: Hazeva Group (17-6 Ma; 6448 – 4700 m depth), Sedom salt (6 - 3 Ma;
455 4700 – 3750 m depth), Melech Sedom (3 – 1 Ma; 3750 – 2950 m depth), Amora 1 Formation (1
456 – 0.7 Ma; 2950 – 2100 m depth), Amora 2 Formation (0.7 – 0.3 Ma; 2100 – 1400 m depth), and
457 Lisan-Samra Formation (0.3 Ma – present; 1400 – 0 m depth). The lithological descriptions are
458 based on the interpretations of Larsen et al. [2002], *Gardosh et al.* [1997], *Calvo and Bartov*
459 [2001], *Horowitz* [1987], *Bartov et al.,* [2002], and *Bartov et al.,* [2007].
460
461 The Hazeva Group, which outcrops at the southern end of the DSB, consists of 5 geologic
462 formations, with the two lowest formations (Ef'e and Gidron) being older than the ~17 Ma age
463 of the DST (as old as 20 Ma [*Calvo and Bartov,* 2001], or 23.8 Ma [*Horowitz*, 1987]). These two
464 formations are <200 m thick and their inclusion in the subsidence calculation introduces only a
465 small error to the subsidence rate. On the other hand, it is not clear if the Sedom Deep-1 well
466 reached the bottom of Hazeva Formation [*Gardosh et al.,* 1997; *Calvo and Bartov,* 2001]. The
467 Sedom Salt Formation in this well consists of 950 m of halite with a mix of anhydrite and
468 gypsum, but the presence of large salt diapirs within the DSB suggests salt migration with time.
469 *Horowitz* [1987] estimated the original thickness of salt layer between 1000-1200 m, and
470 *Garfunkel* [1997] suggested it to be 2000 m. The Sedom Salt formation is calculated using two
471 end member scenarios: one where only 950 m where deposited during the Pliocene and the
472 other, where 2000 m of salt were deposited, but the layer thickness has since been decreasing
473 linearly with time at a rate to the current observed thickness of 950 m.
474
475 The Melech Sedom unit of the Amora Formation consists of 800 m of mostly of quartz
476 sandstones deposited in the late Pliocene-early Pleistocene [*Horowitz*, 1987]. The remaining
477 Pleistocene-age Amora Formation is divided into two sections. The Amora 1 section is an 850-
478 m-thick fining upward deposition sequence with dominant sands interlaced with shales and the

Amora 2 section comprises of 600-m-thick mix of shale and sands overlain by 100 m of mostly shales [*Gardosh et al.,* 1997; *Larsen et al.,* 2002]. The Lisan-Samra Formation consists of a 1400-m-thick sequence of shaley sands with clays and lake carbonates deposited from 0.70 – 0.150 Ma [*Begin*, 1975; *Bartov et al.,* 2002; *Bartov et al.,* 2007]. The surface at Sedom Deep-1 well is currently at ~-380 m. Because of the lack of constraints on the rate of surface subsidence, the entire 380 m were added to the most recent section.

The total tectonic subsidence of the basin (Figure 10) is close to the total thickness of sediments for three reasons: (a) isostatic amplification was not considered; (b) the large time interval represented by the Hazeva Group was de-compacted as a single unit; and (c) the mainly salt layer of Sedom Salt Formation was not de-compacted at all. The subsidence rate appears to have been fairly constant at a few hundred meters/m.y. throughout the life of the basin and has accelerated by an order of magnitude about 1 m.y. ago (Figure 10). Using U-series and oxygen isotope chronology for the mid-Pleistocene, *Torfstein et al.* [2009] suggested that a gypsum layer at a depth of 540 m was deposited 420 ky ago. This depth-age pair implies a slightly lower subsidence rate for the late Pleistocene (grey dot in Figure 10), but this rate is still an order of magnitude higher than the Mio-Pliocene subsidence rate.

Subsidence rates of a few hundred m/m.y. appear to be typical to other basins along the DST. $^{40}Ar/^{39}Ar$ dating of basalt layers in a 2781-m-deep well at the center of the Hula basin (Figure 1) gives a uniform rate of subsidence (not corrected for compaction) of 500-700 m/m.y. since 4.1 Ma [*Heimann and Steinitz*, 1989]. Pollen dating of a 4249-m-deep well in Kinarot basin (Figure 1) gives an uncorrected subsidence rate of 500 m/m.y. since 1.8 Ma and ~300 m/m.y. since Middle Miocene [*Horowitz*, 1987].

In the Dead Sea basin the accelerating subsidence rate during the Pleistocene is supported by geological evidence. Sedimentation during the Miocene has kept up with subsidence as indicated by evidence for occasional sediment transport from east to west across the basin [*Garfunkel and Horowitz,* 1966]. Sands within the Pliocene salt layer were derived from the underlying Hazeva Group sediments, whereas sands in the Amora Formation sample the entire Phanerozoic section

[*Sa'ar*, 1985], indicating that the present topography of a basin and uplifted highlands has mainly developed during the Pleistocene [*ten Brink and Ben-Avraham*, 1989]. The present surface elevation of the lake (-422 m) also suggests that sedimentation has recently not kept up with subsidence. Estimates of subsidence rate from interferometric synthetic aperture radar (InSar) measurements are 0-20 mm/y, although it is difficult to separate consolidation, salt movement, and hydrologic effects from tectonic subsidence [*Baer et al.,* 2002].

5. Discussion – the role of fluids in basin subsidence

Several observations about structure and temporal evolution of the DSB provide important constraints on its mechanical development. 1. The lower crust below 18 km does not appear to be affected by basin development, despite the great depth of the basin (≤8.5 km). 2. Upper crustal P-wave velocity is anomalously low in a narrow (10-15 km) zone beneath the basin. 3. Subsidence rate has accelerated by an order of magnitude during the past 1 m.y.

A decrease in upper crust *P* wave velocity under the basin is interpreted to be the result of higher than typical pore fluid pressure in that layer [e.g., *Stern et al.,* 2001]. The magnitude of the decrease depends on pore geometry; the decrease is small if the pores are round but is significant if pores are thin and long [*Marquis and Hyndman,* 1992]. It is less likely that the reduction in wave speed is due to dry fractures, because dry fractures will likely shut with depth [*Mooney and Ginzburg,* 1986]. The fluid source to the middle crust could be fluids drawn from the surrounding crust by the large negative vertical stress (≤ 45 MPa) under the basin due to its lighter overburden relative to the surrounding areas (Figure 11a), and/or by dehydration of the upper mantle and migration up deep shear zones. *Kennedy et al.* [1997] used $^{3}He/^{4}He$ ratio in wells, springs, and seeps along the San Andreas Fault to suggest that mantle fluids pass through the ductile crust into the brittle fault zone. The helium ratio indicates that between 1%-50% of the surface fluids may originate in the mantle. *Kennedy et al.* [2007] documented a positive regional correlation between $^{3}He/^{4}He$ ratios in surface fluids in the western U.S. and the rate of crustal extension and shear strain. *Friedman et al.* [1999] discussed possible evidence for mantle or lower crust fluids in groundwater along the DST, although a thorough analysis has not been done.

539

540 Retrograde metamorphic reactions of feldspar in the presence of pore fluids have been
541 documented in several shear zones in the middle continental crust [*Beach*, 1980; *Gueydan et al.,*
542 2003; *Janecke and Evans*, 1988]. The metamorphic reactions produce muscovite, which alters
543 the fabric and strength of the deformed rock by producing weak, highly foliated mica bands.
544 Laboratory deformation experiments of thin layers of oriented muscovite aggregate (simulated
545 shear zone) show semi-brittle behavior at low strain rates at temperatures < 700°C, but at 700°C
546 the shear strength falls rapidly with a linear-viscous characteristic [*Mariani et al.,* 2006].
547 Extrapolating these results to geological strain rates (10^{-12}- 10^{-14} s^{-1}), these authors proposed a
548 rapid strength drop by viscous creep at depths of 15-18 km (assuming a temperature gradient of
549 22°C/km and an overburden rate of 27 MPa/km). Laboratory experiments of fine-grained
550 feldspar aggregate at higher pressure and temperatures show that water in isolated pores under
551 hydrostatic conditions changed during deformation to wetted grain boundaries [*Tullis et al.,*
552 1996]. A significant strength drop and an order of magnitude increase in bulk transport rate
553 through the aggregate accompanied the fluid re-distribution, and the deformation mode changed
554 from dislocation creep to diffusion creep. A similar effect was not seen in quartz.
555

556 *Bailey* [1990] proposed that aqueous fluids can percolate rapidly through the ductile lower crust,
557 but are trapped at the brittle-ductile transition within the crust because of the low permeability of
558 the brittle crust. Given the generally compressive state of stress in the continental lithosphere
559 [*Zoback*, 1992], the fluids are expected to accumulate in horizontal layers aided perhaps by
560 hydraulic fracturing. As shown by the $^{3}He/^{4}He$ ratio in the San Andreas Fault [*Kennedy et al.,*
561 1997], the presence of a continental transform zone under the DSB will likely aid in the transport
562 of fluids to the middle crust.
563

564 We propose that the sudden increase in subsidence rate of the DSB is the result of hydration
565 reactions causing retrograde metamorphism of feldspar to muscovite in the middle crust. This
566 alteration helped focus the extension into narrow inter-connected mid-crustal ductile shear zones
567 (Figure 11b) resulting in a significant shear strength reduction and a significant increase in
568 transport rate in that layer. An increase in subsidence rate under the basin can occur if the ductile

shear zones extend horizontally to the crust surrounding the basin and spread the subsidence over a broader region or if the ductile shear zones connect vertically to deeper crustal levels or to shallow low-angle faults.

The connection of mid-crustal shear zones to deeper or shallower levels in continental rifts is expected to result in exhumation of the lower crust and/or upper mantle [e.g., *Lavier and Manatschal*, 2006]. Because there are no observations of lower crustal exhumation and shallow low-angle faults along the DST, ductile shear zones under the DSB are probably confined to the middle crust and distribute the subsidence over a broader region. The clearest example of distributed subsidence is the "sagging" of the basin south of the Amazyahu transverse fault without significant transverse faulting ([*Al-Zoubi and ten brink*, 2002], Figures 1, 6b). *Larsen et al.* [2002] proposed that a southward migration of the depocenter across Amazyahu fault started ~1 m.y. ago. Farther south, the basin gradually thins until it disappears about 50 km to the south. Stratigraphic relationships in this part show possible onlap to the south, which is interpreted as lengthening of the basin with time (Figure 11b). The average Pleistocene subsidence of the southern part is at least 1.25 km [*Al-Zoubi and ten Brink,* 2002]. Other areas of subsidence are more speculative: The central ~80 km of the basin is ~15 km wide, 5 km wider than the gap between the strike-slip fault strands (e.g., Figure 7). The region outside the fault strands consists of subsided blocks of intermediate depth along the west side [*Kashai and Crocker*, 1987; *ten Brink and Ben-Avraham*, 1989] and in places also along the east side [*Al-Zoubi et al.,* 2002]. Post mid-Pleistocene subsidence is estimated to be at least 1.5 km (Amiaz borehole [*Gardosh et al.,* 1997]). The northern 20 km of the basin, where the surrounding blocks of intermediate depth almost disappear (Figure 7), could perhaps accommodate ≤2 km of subsidence, but its geometry and subsidence history are poorly constrained. Lastly, extrapolating GPS rates of motion suggests that the upper crust of the pull-apart basin probably extended by ~5 km during the past 1 m.y. Of the 4-km of subsidence since 1 m.y. ago, ~1 km of subsidence in the central ~80 km of the basin could have been the result of partial evacuation of the Pliocene salt into diapirs [*Garfunkel*, 1997], which may have started in the mid-Pleistocene [*ten Brink and Ben-Avraham,* 1989]. The remaining subsidence can then be balanced by the subsidence south, west, and perhaps north of the deepest part of the basin, and by the predicted extension during that period.

599 Hence, we propose that the increased subsidence rate in the central deep part of the DSB is
600 accommodated by subsidence in a broader region.
601
602 The DSB may not be the only basin where rapid subsidence unrelated to a tectonic event has
603 occurred. For example, an anomalous rapid subsidence phase, accompanied by minor normal
604 faulting was documented in the North Sea around 55 Ma, when the North Atlantic mantle plume
605 reached the earth surface [*White and Latin*, 1993]. That subsidence could not be satisfactory
606 explained by tectonic or isostatic causes [*Hall and White,* 1994]. On the other hand, *White and*
607 *Latin* [1993] summarized evidence for rapid illite diagenesis and the presence of unusually warm
608 saline pore fluids in quartz fluid inclusions within the sediments during that time without
609 commenting on its origin or relationship to the subsidence. Magmas from the Iceland plume
610 have elevated water content [e.g., *Poreda et al.,* 1986]. Hence, it is possible that aqueous fluids
611 related to the mantle plume rose to the middle crust to create mid-crustal ductile shear zone
612 during a minor extension event, perhaps itself driven by the rising plume.
613
614 We propose that the rapid subsidence starting 1 m.y. ago is a culmination of slow fluid migration
615 into the middle crust and micro faulting there for many millions of years as the basin deepened
616 and the transform fault continued to be active in the same location. Aqueous fluids can be drawn
617 from the deeper crust and mantle and from the surrounding crust into the middle crust under the
618 DSB by the large negative vertical stress (≤ 45 MPa) under the basin due to its lighter
619 overburden relative to the surrounding areas (Figure 11a**).** A positive feedback exists during the
620 extension process, which helps concentrate fluids at the base of the quartzo-feldspatic crust as
621 the basin continues to deepen and the overburden to lighten. Micro-faulting and fracturing of the
622 crust during the millions of years of seismic activity along the DST further facilitates fluid
623 accumulation under the basin.
624
625 An alternative explanation for the 4 km of subsidence of the DSB in the past ~1 m.y. is that a
626 change in relative plate motions in the Eastern Mediterranean region at that time [*Schattner and*
627 *Weinberger*, 2008] has resulted in a small component of extension across the basin. However,
628 because the pole of rotation between Arabia and Africa (or the Sinai block) is close to the plate

boundary and is not well constrained, different solutions may produce different senses of motion across the basin [*Le Beon et al.,* 2008]. Moreover, the internal stratal relationships of the shallow basin fill do not show evidence for E-W extension [e.g., *Al-Zoubi et al.,* 2002; *Larsen et al.,* 2002]. The continued rise of the Sedom salt diapir above the surface [*Weinberger et al.,* 2006] requires, in fact, the presence of a slight E-W compression, as discussed by *Al-Zoubi and ten Brink* [2001]. The recent increase in subsidence rate does not represent thermal subsidence, because the basin is narrow and any increase in thermal gradient due to mantle upwelling is continuously offset by lateral heat conduction to the surrounding area [*Pitman and Andrews,* 1985; *ten Brink et al.,* 1993].

Another alternative explanation to the 4 km of subsidence in the past 1 m.y. is an increase of mantle heat flux that has not yet reached the surface. *Moshen et al.* [2006] determined a thinner than normal (70-80 km) lithosphere from receiver-function analysis and suggested that it reflects late Cenozoic thinning. *Al-Damegh et al.* [2004] mapped a zone of high *Sn* attenuation along the eastern side of the Dead Sea fault system. A thinner and hotter lithosphere under the DSB than is expected from surface heat flow, could result in lower viscosity and the onset of lower crust flow. However, the detection of earthquake hypocenters within the lower crust [*Aldersons et al.,* 2003; *Braeuer et al.*, submitted] argues against a hot lower crust. Micro-seismicity in the lower crust can be understood however, in the context of rapidly rising fluids in the lower crust. If the ascent rate is fast enough, fluids can locally create hydro-fracturing even within the ductile crust, and thinning of the lithosphere could also promote the production of aqueous fluids.

6. Conclusions

Based on the information and interpretations presented above as well as other published studies, we characterize the structure and evolution of the DSB as follows:

1. The basin is up to 8-8.5 km deep under the Lisan Peninsula. Previous estimates of the maximum depth of the basin using gravity did not consider lower density in the upper crust under the basin and hence required a thicker basin fill to explain the added negative gravity anomaly.

2. The basin extends 50 km farther south of the only significant transverse normal fault, and gradually shallows without significant brittle deformation. The internal stratigraphy of the basin fill suggests that the basin proceeded to elongate southward with time after its formation [*Al-Zoubi and ten Brink,* 2002].
3. The shape of the northern termination of the basin is not well determined. Gravity modeling suggests gradual thinning toward the northern end of the lake (Figure 6b, 7). Tomographic inversion, on the other hand, suggests that the basin continues to be 6 km deep to the northern end of the lake (Figure 6b, 8) where it abruptly thins, but the spatial resolution of the tomography is probably no better than 25 km. There is no clearly imaged transverse fault at the northern end of the lake although one was suggested [*Neev and Hall,* 1979; *ten Brink and Ben-Avraham,* 1989; *Lazar et al.,* 2006]. A 2-D ray-tracing model (Figure 9a) shows the basin depth as < 2.5 km immediately north of the lake thinning to 1.5 km 50 km to the north.
4. The underlying pre-basin sedimentary layer thickens gradually under the DST from 2-3 km under the southern edge of the DSB to 3-4 km under the northern end of the lake and 5-6 km farther north. At the deepest part of the basin under the Lisan, the pre-basin sediments reach a depth of ~11 km. The layer's lithology changes from predominantly clastic east and south of the DSB to carbonate west and north of the DSB. The thickness and lithology reflect the location of the DSB at a bend of the Triassic-Jurassic passive continental margin of the Tethys Ocean.
5. The upper crust under the deep part of the basin has a lower *P* wave velocity than in the surrounding regions. Within the data resolution, the lower crust below ~18 km and the Moho are not affected by basin development.
6. The basin started forming during or shortly after the development of the DST ~17 Ma. Subsidence rate was several hundreds m/m.y. for most of that period, similar to other basins along the DST, but subsidence rate has accelerated by an order of magnitude during the Pleistocene or perhaps only in the past 1 m.y.

We explain the anomalously low velocity in the upper crust under the basin, the apparent sagging and extension of the basin, and the rapid subsidence in the past 1 m.y., by the influx of

fluids from the surrounding crust and/or the upper mantle into the middle crust, where these fluids interacted with fractured feldspar to alter some of the feldspar to muscovite. The generation of interconnected muscovite shear bands profoundly weakened the yield strength in this part of the crust and allowed sub-horizontal viscous deformation, and a significant increase in the rate of horizontal transport. These caused the basin to subside rapidly with only minor attendant brittle faulting. We propose that the enigmatic rapid Tertiary subsidence of the North Sea could have been generated by a similar mechanism. Thus, we propose that aqueous fluid flux into a slowly extending continental crust can cause rapid basin subsidence that may be erroneously interpreted as an increased rate of tectonic activity.

Several observations can possibly test the hypothesis that the recent acceleration in subsidence rate is driven by the development over mid-crustal shear zones. These observations include geochemical and petrologic work to examine evidence for potential influx of lower crust and upper mantle aqueous fluids, identifying episodic micro-seismic activity near the base of the upper crust using a semi-permanent network of seismometers around the basin, and obtaining higher-resolution seismic stratigraphy south of Amazyahu Fault to determine the geometry and rate of sagging. Continuous geodetic monitoring of surface subsidence south of Amazyahu Fault and north of the lake may also help detect extension episodes. Finally, deeper penetrating seismic reflection observations of the northern basin, and seismic tomography with more regularly spaced seismic sources and receivers, will improve the constraints on the geometry of the DSB.

Acknowledgments:

Fieldwork was funded by US-AID Middle Eastern Regional Cooperation Program grant M21-012, with in-kind contributions by Al-Balqa' Applied University (Jordan), the Geophysical Institute of Israel, and the U.S. Geological Survey. Abdallah Al-Zoubi, Yair Rotstein, and Randy Keller helped coordinate the project. IRIS and the University of Texas, El Paso, kindly provided seismic equipment. Steve Harder and Isam Qabbani coordinated the field deployment, and Jordanian and Israeli crews, Matt Averill, Galen Kaip, and Tip Meckel provided field support. We thank Moshe Reshef for discussion and information. Discussions with Tim Stern

718 substantially improved the manuscript. Tim Stern, Carolyn Ruppel, Uri Schattner, an anonymous
719 reviewer, and associate editor Gail Christeson provided helpful reviews.
720

721 **References**

722 Abu Saad, L., and I. J. Andrews (1993), A database of stratigraphic information from deep
723 boreholes in Jordan, *Subsurface Geology Bull., Nat. Resources Auth., Jordan*, *6*, 1-182.
724 Abu-Ajamieh, M. M., F. K. Bender, R. N. Eicher, K. K. El-Kaysi, F. Nimri, B. H. Qudah, and K.
725 H. Sheyyab (1988), *Natural resources in Jordan; inventory, evaluation, development*
726 *program*, 308 pp., Jordan Natural Resources Authority, Amman, Jordan.
727 Al-Damegh, K., E. Sandvol, A. Al-Lazki, and M. Barazangi (2004), Regional seismic wave
728 propagation (Lg and Sn) and Pn attenuation in the Arabian Plate and surrounding regions,
729 *Geophys. J. Int.*, 15, 775-795.
730 Al-Tarazi, E., E. Sandvol, and F. Gomez (2006), The February 11, 2004 Dead Sea earthquake M
731 (super L) 5.2 in Jordan and its tectonic implication, *Tectonophys.*, *422*, 149-158.
732 Al-Zoubi, A., and U. S. ten Brink (2001), Salt diapirs in the Dead Sea basin and their
733 relationship to Quaternary extensional tectonics, *Mar. Petrol. Geol.*, *18*, 779-797.
734 Al-Zoubi, A., and U. S. ten Brink (2002), Lower crustal flow and the role of shear in basin
735 subsidence; an example from the Dead Sea basin, *Earth Planet. Sci. Lett.*, *199*, 67-79.
736 Al-Zoubi, A., H. Shulman, and Z. Ben-Avraham (2002), Seismic reflection profiles across the
737 southern Dead Sea basin, *Tectonophys.*, *346*, 61-69.
738 Al-Zoubi, A. S., T. Heinrichs, I. Qabbani, and U. S. ten-Brink (2007), The northern end of the
739 Dead Sea basin; geometry from reflection seismic evidence, *Tectonophys.*, *434*, 55-69.
740 Aldersons, F., Z. Ben-Avraham, A. Hofstetter, E. Kissling, and T. Al-Yazjeen (2003), Lower-
741 crustal strength under the Dead Sea basin from local earthquake data and rheological
742 modeling, *Earth Planet. Sci. Lett.*, *214*, 129-142.
743 Andrews, I. J. (1991), Palaeozoic lithostratigraphy in the subsurface of Jordan *Rep.*, *Subsurface*
744 *Geology Bull.* 2, 75 pp., Nat. Resources Auth., Jordan.
745 Andrews, I. J. (1992a), Permian, Triassic and Jurassic lithostratigraphy in the subsurface of
746 Jordan*Rep.*, 60 pp, *Subsurface Geology Bull.* 4, 60 pp.*, Nat. Resources Auth., Jordan*,
747 Andrews, I. J. (1992b), Cretaceaus and Paleogene lithostratigraphy in the subsurface of Jordan,
748 *Subsurface Geology Bull.* 5, 60 pp., Nat. Resources Auth., Jordan,
749 Arbenz, J. K. (1984), *Oil potential of the Dead Sea area, Report 84/111*, Seismica Oil
750 Exploration Ltd. , Tel Aviv.

751 Aydin, A., and A. Nur (1982), Evolution of pull-apart basins and their scale independence,
752 *Tectonics*, *1*, 91-105.
753 Baer, G., U. Schattner, D. Wachs, D. Sandwell, S. Wdowinski, and S. Frydman (2002), The
754 lowest place on Earth is subsiding; an InSAR (interferometric synthetic aperture radar)
755 perspective, *Geol. Soc. Am. Bull.*, *114*, 12-23.
756 Bailey, R. C. (1990), Trapping of aqueous fluids in the deep crust, *Geophys. Res. Lett.*, *17*, 1129-
757 1132.
758 Bartov, Y., Y. Enzel, N. Porat, M. Stein (2007), Evolution of the late Pleistocene-Holocene
759 Dead Sea basin from sequence stratigraphy of fan deltas and lake-level reconstruction, *J.*
760 *Sediment. Res.*, 77, 680-692.
761 Bartov, Y., M. Stein, Y. Enzel, A. Agnon, Z. Reches (2002), Lake Levels and Sequence
762 Stratigraphy of Lake Lisan, the Late Pleistocene Precursor of the Dead Sea, *Quarter. Res.*,
763 57, 9-21, doi: 10.1006/qres.2001.2284.
764 Beach, A. (1980), Retrogressive metamorphic processes in shear zones with special reference to
765 the Lewisian complex, *J. Struct. Geol.*, *2*, 257-263.
766 Begin, Z.B., Paleocurrents in the Plio-Pleistocene Samra Formation (Jericho Region, Israel) and
767 Their Tectonic Implication, *Sed. Geol.*, 14, 191-218, 1975.
768 Ben-Avraham, Z., and G. Schubert (2006), Deep "drop down" basin in the southern Dead Sea,
769 *Earth Planet. Sci. Lett.*, *251*, 254-263.
770 Bender, F. (1974), *Geology of Jordan*, 196 pp., Gebrueder Borntraeger, Berlin.
771 Braeuer, B., G. Asch, R. Hofstetter, Ch. Haberland, D. Jaser, R. el-Kelani, and M. Weber,
772 Microseismicity distribution in the southern Dead Sea area and its implications on the
773 structure of the basin, *Geophys. J. Int.,* submitted.
774 Brocher, T. M. (2005), Empirical relations between elastic wavespeeds and density in the Earth's
775 crust, *Bull. Seismol. Soc. Am.*, *95*, 2081-2092.
776 Calvo, R., and Y. Bartov (2001), Hazeva Group, southern Israel; new observations, and their
777 implications for its stratigraphy, paleogeography, and tectono-sedimentary regime, *Isr. J.*
778 *Earth Sci.*, *50*, 71-99.
779 Crowell, J. C. (1974), Sedimentation along the San Andreas Fault, California, *Spec. Pub. Soc.*
780 *Econ. Paleontol. Mineral.*, *19*, 292-303.

781 Eckstein, Y., and G. Simmons (1978), Measurements and interpretation of terrestrial heat flow in
782 Israel, *Geothermics*, *6*, 117-142.
783 Freund, R., Z. Garfunkel, I. Zak, M. Goldberg, T. Weissbrod, and B. Derin (1970), The shear
784 along the Dead Sea rift: A discussion on the structure and evolution of the Red Sea and the
785 nature of the Red Sea, Gulf of Aden and Ethiopia rift junction, *Philos. Trans. Roy. Soc.*
786 *London, Series A, 267*, 107-130.
787 Friedman, G. M., H. Gvirtzman, G. Garven, and G. Gvirtzman (1999), Thermal anomalies
788 associated with forced and free ground-water convection in the Dead Sea Rift valley;
789 discussion and reply, *Geolog. Soc. Am. Bull.*, *111*, 1098-1102.
790 Galanis, S. P., Jr., J. H. Sass, R. J. Munroe, and M. Abu-Ajamieh (1986), Heat flow at Zerqa
791 Ma'in and Zara and a geothermal reconnaissance of Jordan, *USGS Open-File Report*, *86-631*,
792 1-110.
793 Gardosh, M., E. Kashai, S. Salhov, H. Shulman, and E. Tannenbaum (1997), Hydrocarbon
794 exploration in the southern Dead Sea basin, in *The Dead Sea: The lake and its setting*, edited
795 by T. M. Niemi, et al., pp. 57-72, Oxford University Press, Oxford.
796 Garfunkel, Z., and B. Derin (1984), Permian early Mesozoic tectonism and continental margin
797 formation in Israel and its implications of the history of the eastern Mediterranean, *Geol.*
798 *Soc. Lond. Spec. Pub.* 17, 187-201.
799 Garfunkel, Z., and A. Horowitz (1966), The upper Tertiary and Quaternary morphology of the
800 Negev, Israel, *Isr. J. Earth Sci.*, *15*, 101-117.
801 Garfunkel, Z., and Z. Ben-Avraham (1996), The structure of the Dead Sea basin, *Tectonophys.*,
802 *266*(1-4), 155-176.
803 Garfunkel, Z. (1997), The history and formation of the Dead Sea basin, *Oxford Monographs on*
804 *Geology and Geophysics*, *36*, 36-56.
805 Gilboa, Y., H. Fligelman, B. Derin, N. H. Foster, and E. A. Beaumont (1993), Zohar-Kidod-
806 Haqanaim fields; Israel, eastern Mediterranean Basin, *AAPG Treatise of Petroleum Geology,*
807 *Atlas of Oil and Gas Fields*, *A-26*, 129-152.
808 Ginzburg, A., and Z. Ben-Avraham (1997), A seismic refraction study of the north basin of the
809 Dead Sea, Israel, *Geophys. Res. Lett.*, *24*, 2063-2066.

Ginzburg, A., J. Makris, K. Fuchs, B. Perathoner, and C. Prodehl (1979), Detailed structure of the crust and upper mantle along the Jordan-Dead Sea rift, *J. Geophys. Res.*, *84*, 5605-5612.

Ginzburg, A., M. Reshef, Z. Ben-Avraham, and U. Schattner (2007), The style of transverse faulting in the Dead Sea basin from seismic reflection data: The Amazyahu fault, *Isr. J. Earth Sci.*, *55*, 129-139.

Gueydan, F., Y. M. Leroy, L. Jolivet, and P. Agard (2003), Analysis of continental midcrustal strain localization induced by microfracturing and reaction-softening, *J. Geophys. Res.*, *108*, 2064, doi:10.1029/2001JB000611.

Haberland, C., N. Maercklin, D. Kesten, T. Ryberg, C. Jannsen, A. Agnon, M. Weber, A. Schulze, I. Qabbani, and R. El-Kelani (2007), Shallow architecture of the Wadi Araba fault (Dead Sea Transfrom) from high-resolution seismic investigations, *Tectonophys.*, *432*, 37-50.

Hall, B. D., and N. White (1994), Origin of anomalous Tertiary subsidence adjacent to North Atlantic continental margins, *Mar. Petrol. Geol.*, *11*, 702-714.

Hölzel, M., R. Faber, M. Wagreich (2008), DeCompactionTool: Software for subsidence analysis including statistical error quantification, *Computers & Geosciences*, 34, 1454-1460.

Horowitz, A. (1987), Palynological evidence for the age and rate of sedimentation along the Dead Sea Rift, and structural implications, *Tectonophys.,* 141, 107-115.

Janecke, S. U., and J. P. Evans (1988), Feldspar-influenced rock rheologies, *Geology*, *16*, 1064-1067.

Kashai, E. L., and P. F. Croker (1987), Structural geometry and evolution of the Dead Sea-Jordan rift system as deduced from new subsurface data, *Tectonophys.,* 141, 33-60.

Katzman, R., U. S. ten Brink, and J. Lin (1995), Three-dimensional modeling of pull-apart basins; implications for the tectonics of the Dead Sea Basin, *J. Geophys. Res., 100*, 6295-6312.

Kennedy, B. M., Y. K. Kharaka, W. C. Evans, A. Ellwood, D. J. De Paolo, J. J. Thordsen, G. Ambats, and R. H. Mariner (1997), Mantle fluids in the San Andreas fault system, California, *Science*, *278*, 1278-1281.

Kennedy, B. M., and M. C. van Soest (2007), Flow of mantle fluids through the ductile lower crust; helium isotope trends, *Science*, *318*, 1433-1436.

840 Klein, F. W. (2002), User's guide to HYPOINVERSE-2000, a Fortran program to solve for
841 earthquake locations and magnitudes, 123 pp, Reston, VA.
842 Larsen, B.D., Z. Ben-Avraham, H. Shulman (2002), Fault and salt tectonics in the southern Dead
843 Sea basin, *Tectonophys.,* 346, 71-90.
844 Lavier, L.L., and G. Manatschal (2006), A mechanism to thin the continental lithosphere at
845 magma-poor margins, *Nature*, *440*, 324-328.
846 Lazar, M., Z. Ben-Avraham, and U. Schattner (2006), Formation of sequential basins along a
847 strike-slip fault; geophysical observations from the Dead Sea basin, *Tectonophys.*, *421*, 53-
848 69.
849 Le Beon, M., and 8 others (2008), Slip rate and locking depth from GPS profiles across the
850 southern Dead Sea Transform, *J. Geophys. Res.,* 113, B11403, doi:10.1029/2007JB005280.
851 Mariani, E., K. H. Brodie, and E. H. Rutter (2006), Experimental deformation of muscovite
852 shear zones at high temperatures under hydrothermal conditions and the strength of
853 phyllosilicate-bearing faults in nature, *J. Struct. Geol.*, *28*, 1569-1587.
854 Marquis, G., and R. D. Hyndman (1992), Geophysical support for aqueous fluids in the deep
855 crust; seismic and electrical relationships, *Geophys. J. Int.*, *110*, 91-105.
856 May, S. R., K. D. Ehman, G. G. Gray, and J. C. Crowell (1993), A new angle on the tectonic
857 evolution of the Ridge basin, a "strike-slip" basin in southern California, *Geol. Soc. Am.*
858 *Bull.*, *105*, 1357-1372.
859 Mechie, J., K. Abu-Ayyash, Z. Ben-Avraham, R. El-Kelani, A. Mohsen, G. Ruempker, J. Saul,
860 and M. Weber (2005), Crustal shear velocity structure across the Dead Sea transform from
861 two-dimensional modelling of DESERT project explosion seismic data, *Geophys. J. Int.*,
862 *160*, 910-924.
863 Mechie, J., K. Abu-Ayyash, Z. Ben-Avraham, R. El-Kelani, I. Qabbani, and M. Weber (2009),
864 Crustal structure of the southern Dead Sea basin derived from Project DESIRE wide-angle
865 seismic data, *Geophys. J. Int.*, *178*, 457-478.
866 Mohsen, A., R. Kind, S. V. Sobolev, M. Weber, and t. D. Group (2006), Thickness of the
867 lithosphere east of the Dead Sea Transform, *Geophys. J. Int.*, *167*, 845-852.
868 Mooney, W.D. and A. Ginzburg (1986), Seismic properties of the internal properties of fault
869 zones, PAGEOPH, 124, 141-156.

870 Neev, D. and J.K. Hall (1979), Geophysical Investigations in the Dead Sea, Sedimentary
871 Geology, 23, 209 – 238.
872 Petrunin, A., and S. V. Sobolev (2006), What controls thickness of sediments and lithospheric
873 deformation at a pull-apart basin?, *Geology*, *34*, 389-392.
874 Petrunin, A. G., and S. V. Sobolev (2008), Three-dimensional numerical models of the evolution
875 of pull-apart basins, *Phys. Earth Planet. Interiors*, *171*, 387-399.
876 Pitman, W. C., III, and J. A. Andrews (1985), Subsidence and thermal history of small pull-apart
877 basins, *Soc. Econo. Paleontol. Mineral. Spec. pub.*, *37*, 45-119.
878 Poreda, R., J. G. Schilling, and H. Craig (1986), Helium and hydrogen isotopes in ocean-ridge
879 basalts north and south of Iceland, *Earth Planet. Sci. Lett.*, *78*, 1-17.
880 Quennell, A. M. (1958), The structural and geomorphic evolution of the Dead Sea rift, *Quarterly*
881 *J. Geol. Soc. Lond.*, *114, Part 1*, 1-24.
882 Regenauer-Lieb, K., G. Rosenbaum, and R. F. Weinberg (2008), Strain localisation and
883 weakening of the lithosphere during extension, *Tectonophys.*, *458*, 96-104.
884 Rybakov, M., V. Goldshmidt, Y. Rotstein, L. Fleischer, I. Goldberg, C. Campbell, and P.
885 Millegan (1999), Petrophysical constraints on gravity/magnetic interpretation in Israel,
886 *Leading Edge*, 18, 269-272, Tulsa, OK.
887 Rybakov, M., and A. Segev (2004), Top of the crystalline basement in the Levant, *Geochem.,*
888 *Geophys., Geosys.*, *5*(9) doi:10.1029/2004gc000690.
889 Sa'ar, H. (1985), Origin and sedimentation of sandstones in graben fill formations of the Dead
890 Sea rift valley, Rep. MM/3/86, Geol. Survey Isr., Jerusalem.
891 Seeber, L., M. Cormier, C. McHugh, O. Emre, A. Polonia, and C. Sorlien (2006), Rapid
892 subsidence and sedimentation from oblique slip near a bend on the North Anatolian
893 transform fault in the Marmara Sea, Turkey, *Geology*, *34*, 933-936.
894 Segall, P., and D. D. Pollard (1980), Mechanics of discontinuous faults, *J. Geophys. Res.*, *85*,
895 4337–4350.
896 Segev, A., M. Rybakov, V. Lyakhovsky, A. Hofstetter, G. Tibor, V. Goldshmidt, and Z. Ben
897 Avraham (2006), The structure, isostasy and gravity field of the Levant continental margin
898 and the southeast Mediterranean area, *Tectonophys.*, *425*, 137-157.

899 Schattner, U., and R. Weinberger (2008), A mid-Pleistocene deformation transition in the Hula
900 Basin, northern Israel; implications for the tectonic evolution of the Dead Sea Fault,
901 *Geochem., Geophys., Geosys.*, *9*(7), Q07009. doi:10.1029/2007GC001937.
902 Song, J.-L., and U. ten Brink (2004), A graphical user interface for interactive forward and
903 inversion ray-tracing, 33 pp, U.S. Geological Survey, Reston, VA.
904 Shamir, G., Y. Eyal, and I. Bruner (2005), Localized versus distributed shear in transform plate
905 boundary zones: The case of the Dead Sea Transform in the Jericho Valley, *Geochem.,*
906 *Geophys., Geosys.*, *6*(5), Q05004. doi:10.1029/2004GC000751.
907 Steckler, M. S., and A. B. Watts (1978), Subsidence of the Atlantic-type continental margin off
908 New York, *Earth Planet. Sci. Lett.*, *41*, 1-13.
909 Stern, T. A., S. Kleffman, D. A. Okaya, M. Scherwath, and S. Bannister (2001), Low seismic-
910 wave speeds and enhanced fluid pressure beneath the Southern Alps of New Zealand,
911 *Geology*, *29*, 679-682.
912 ten Brink, U. S., and Z. Ben-Avraham (1989), The anatomy of a pull-apart basin: Seismic
913 reflection observations of the Dead Sea basin, *Tectonics*, *8*, 333-350.
914 ten Brink, U. S., Z. Ben-Avraham, R. E. Bell, M. Hassouneh, D. F. Coleman, G. Andeasen, G.
915 Tibor, and B. Coakley (1993), Structure of the Dead Sea pull-apart basin from gravity
916 analysis, *J. Geophys. Res.*, *98*, 21887-21894.
917 ten Brink, U. S., R. Katzman, and J. Lin (1996), Three-dimensional models of deformation near
918 strike-slip faults, *J. Geophys. Res.*, *101*, 16,205-216,220.
919 ten Brink, U. S., M. Rybakov, A. S. Al-Zoubi, M. Hassouneh, U. Frieslander, A. T. Batayneh, V.
920 Goldschmidt, M. N. Daoud, Y. Rotstein, and J. K. Hall (1999), Anatomy of the Dead Sea
921 Transform; does it reflect continuous changes in plate motion?, *Geology*, *27*, 887-890.
922 ten Brink, U. S., A. S. Al-Zoubi, C. H. Flores, Y. Rotstein, I. Qabbani, S. H. Harder, and G. R.
923 Keller (2006), Seismic imaging of deep low-velocity zone beneath the Dead Sea basin and
924 transform fault; implications for strain localization and crustal rigidity, *Geophys. Res. Lett.*,
925 *33*(24), L24314 doi:10.1029/2006GL027890.
926 ten Brink, U. S., M. Rybakov, A. S. Al-Zoubi, and Y. Rotstein (2007), Magnetic character of a
927 large continental transform; an aeromagnetic survey of the Dead Sea Fault, *Geochem.,*
928 *Geophys., Geosys.*, *8*(7), Q07005, doi:10.1029/2007GC001582.

929 Torfstein, A., A. Haase-Schramm, N. Waldmann, Y. Kolodny, and M. Stein (2009), U-series and
930 oxygen isotope chronology of the mid-Pleistocene Lake Amora (Dead Sea basin),
931 *Geochimica et Cosmochimica Acta*, *73*, 2603-2630.
932 Tullis, J., R. Yund, and J. Farver (1996), Deformation-enhanced fluid distribution in feldspar
933 aggregates and implications for ductile shear zones, *Geology*, *24*, 63-66.
934 White, N., and D. Latin (1993), Subsidence analyses from the North Sea "triple-junction", *J.*
935 *Geol. Soc. Lond.*, *150*, 473-488.
936 Wu, J. E., K. McClay, P. Whitehouse, and T. Dooley (2009), 4D analogue modelling of
937 transtensional pull-apart basins, *Mar. Petrol. Geol.*, *26*, 1608-1623.
938 Zelt, C. A., and R. B. Smith (1992), Seismic traveltime inversion for 2-D crustal velocity
939 structure, *Geophys. J. Int.*, *108*, 16–34.
940 Zelt, C. A., and P. J. Barton (1998), Three-dimensional seismic refraction tomography; a
941 comparison of two methods applied to data from the Faeroe Basin, *J. Geophys. Res.*, *103*,
942 7187-7210.
943 Zoback, M. L. (1992), The World Stress Map Project, *J. Geophys. Res.*, *97*, 11,703-712,013.
944

945

946 **Figure captions**

947 **Figure 1**. Location of deployed seismometers (black) and explosions (red circles) detonated as
948 part of the 2004 active source experiment plotted on shaded relief topography. Red stars – other
949 mining explosions and earthquakes that were recorded during the 2-day deployment and used in
950 the tomography. Numbers correspond to source locations in Table 1. Dashed rectangle defines
951 the area of the tomogrpahic grid. Red lines – Fault geometry simplified from *ten Brink et al.*
952 [1999]. SD-1 – Sedom Deep-1 hole. (Inset) Simplified tectonic map of the Middle East.

953

954 Figure 2 - Observed (in black) and calculated (in red) travel times for sources used for the
955 modeling the W-E line. See Figure 1 for source location.

956

957 Figure 3 – (A) Ray coverage for diving waves (red) and wide-angle reflections in the model
958 (black). (B) Bottoming points for the rays in (A).

959

960 Figure 4 - Receiver gathers for sample sources. See Table 1 for locations. The complete data is
961 shown in Figure A3 in the supplementary material. The gathers were plotted with no time
962 reduction. Receivers 1 to 409 were aligned from south to north and receivers 410 to 755 were
963 aligned from west to east. Red line – first arrival pick for tomography.

964

965 Figure 5 – (A) Ray-path coverage for various shot-receiver distances binned at shot-receiver
966 increments of 20 km. Additional binned increments are found in Figure A4 in the supplementary
967 material. Color dots indicate midpoints for each ray path. Note the uneven coverage due to the
968 locations of all the receivers along two lines (except for a few permanent stations of the Israeli
969 seismic network), and the locations of 14 of the sources at or near these two lines. (B) Depth
970 slices in the checkerboard test. Top – Perturbations in the final velocity model by higher and
971 lower velocities in a checkerboard pattern. Bottom – recovered model. Detailed discussion of the
972 technique and additional depth slices are given in the supplementary material and Figure A5.

973

Figure 6. (a) Top - Comparison between calculated and observed free-air gravity anomaly along the E-W seismic profile (bottom). Density model was derived from the *P* wave velocity model using velocity/density relationships of *Brocher et al.* [2005]. Misfit between calculated and observed anomalies in eastern Jordan may be caused by negative anomaly from Al-Jafr basin south of profile. Bottom - *P* wave velocity contours along the east-west receiver profile from a 2-D ray-tracing model (Figure 1). Red lines – selected velocity contours from the 3-D tomographic model. Colored bodies – interpreted structure: Dark yellow – basin fill; Light yellow – pre-basin fill sediments; Green – upper crust; Orange – lower crust. Stars – controlled explosions. Vertical blue line – depth of Sedom Deep-1 (SD-1) well. Inset – Comparison of basin-fill velocity along the blue line (red) with sonic-log velocity of Sedom Deep-1 well (black). (b) Top – Observed Free-air anomaly along profile in bottom and calculated gravity anomaly using 2.5-D density model shown in Figure 7. Bottom – Contours of *P* wave velocity from a slice of the 3-D tomography model along the center of the Dead Sea Transform valley. Thin lines - bodies in gravity model with density values (red) in 10^3 kg/m^3. Colored bodies – same as in (a) with additional bodies: light blue – salt layer; dark blue – lake water (with a density of 1280 kg/m^3). Shape of Lisan salt diapir is approximate after *Al-Zoubi and ten Brink* [2001]. Dashed colored lines – depth to basin floor and where available, to crystalline basement from previous seismic data (Red – *Al-Zoubi and ten Brink*, 2002; purple – *Ginzburg et al.*, 2007; Green – *Al-Zoubi and ten Brink*, 2001; Blue – *Ginzburg and Ben-Avraham*, 1997). Black crosses – Depth to basement and lower crust in 3 perpendicular seismic refraction profiles: DESERT [*Mechie et al.*, 2005], E-W line ([*ten Brink et al.*, 2006] and Figure 6a) and DESIRE [*Mechie et al.*, 2009]. Dashed brown double-sided arrow bounded by brown dashed horizontal lines – Depth range of most micro-earthquakes in this part of the basin [*Braeuer et al.*, submitted], A.F. – Amazyahu Fault; K.F. – Kalia Fault (proposed by *Lazar et al.* [2006]).

Figure 7. Three slices 2.5-D N-S density model for Figure 6b, west of the transform valley, along of the valley and east. The main sedimentary layers along the transform valley are also outlined on the East and West profiles. Arrows indicate the total width of the density structure over the transform valley. Densities within the basin fill are shown in Figure 6b. See legend for pre-basin sediment density (in 10^3 kg/m^3). Crustal densities increase with depth throughout the

model with values (in 10^3 kg/m^3) in white. Upper crustal densities in a 10-km-wide zone under the basin are lower than in the rest of the model by the shown amount. The 2.5-D model accounts for higher densities east and west of the narrow transform valley. It uses the available constraints from surface and subsurface geology, seismic reflection data, and tomographic analysis, as discussed in text.

Figure 8. Depth (in km) to (a) 5.4 km/s and (b) 5.8 km/s velocity contours from the tomography model. Contours are plotted on top of a Bouguer gravity anomaly map. Red triangles – seismic receivers. Circles – location of controlled explosions. Stars – Quarry explosions. An outline of Dead Sea shoreline in 1965 and rivers are shown in white for reference. The 5.4 km/s contour is interpreted as a proxy for the basin floor and the 5.8 km/s contour as the top of crystalline basement. Bouguer anomaly map is used to qualitatively define the extent of the basin.

Figure 9. *P* wave velocity model along the transform valley (a) south of Amazyahu fault and (b) north of the lake. Colors are *P* wave velocities gridded from the 2-D ray-tracing model. Black lines are layer boundaries used in the model and do not always have geologic significance. Purple dashed lines – base of basin fill and crystalline basement from the gravity model in Figure 6b. Stars – controlled explosions. High velocity around km 260 probably corresponds to the base of a basalt outcrop of Ghor Katar [*Begin*, 1975; *Bender*, 1974], which may also be manifested as a local peak in the gravity profile (Figure 6b). (c) location map.

Figure 10 – Subsidence and subsidence rate curves with estimated error bars for the Dead Sea basin constructed from Sedom Deep-1 borehole Gamma-ray log [*Larsen et al.,* 2002]. See text for details. Subsidence is shown only for the past 7 m.y., because the Hazeva Group (~17-6 Ma) was undivided. Subsidence rate is plotted at the center of the time interval. Red curve – Scenario in which the current thickness of the Sedom Salt layer (950 m) is similar to the deposited thickness. Blue curve – Scenario in which the original thickness of salt layer was 2 km [*Garfunkel*, 1997] and the thickness decreased linearly to its present value by flow and diapirism. Grey curve and dot– Approximate subsidence and subsidence rate for the section described and dated by *Torfstein et al.* [2009].

Figure 11 – (a) Density difference (in 10^3 kg/m^3) between the sediment column within the DSB and a reference column west of the basin. The density difference results in a 45 MPa difference in vertical overburden between the basin and the surrounding region on the west in the middle crust. The difference with the east side is even larger because of the higher elevation and thinner sediment cover east of the basin relative to west of the basin. (b) Sketch of possible mode of crustal extension during the past 1 m.y. The activity on the Amazyahu transverse fault (A.F.) may have decreased. Crustal extension is suggested to be mostly centered in narrow interconnected mica-rich shear bands and perhaps inclined semi-brittle shear bands above them, but subsidence is distributed beyond the central deep basin (km 50-130). K.F. – proposed Kalia fault.

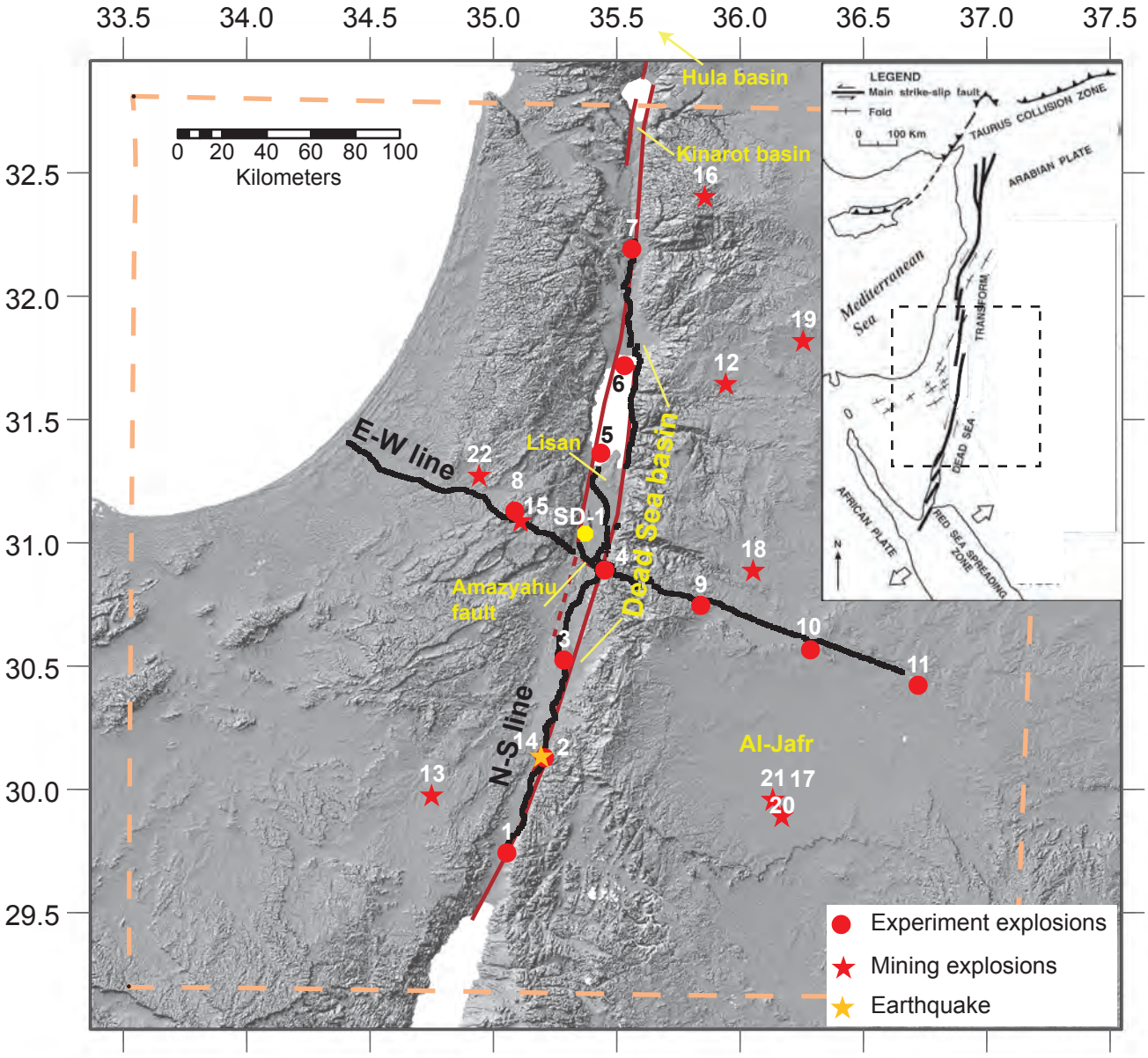
33.5
34.0
34.5
35.0
35.5
36.0
36.5
37.0
37.5
32.5
32.0
31.5
31.0
30.5
30.0
29.5
0 20 40 60 80 100
Kilometers
Hula basin
Kinarot basin
Lisan
Dead Sea basin
E-W line
N-S line
SD-1
Amazyahu fault
Al-Jafr
1
2
3
4
5
6
7
8
9
10
11
12
13
14
15
16
17
18
19
20
21
22
LEGEND
Main strike-slip fault
Fold
0 100 Km
TAURUS COLLISION ZONE
ARABIAN PLATE
Mediterranean Sea
TRANSFORM
DEAD SEA
AFRICAN PLATE
RED SEA SPREADING ZONE
N
Experiment explosions
Mining explosions
Earthquake

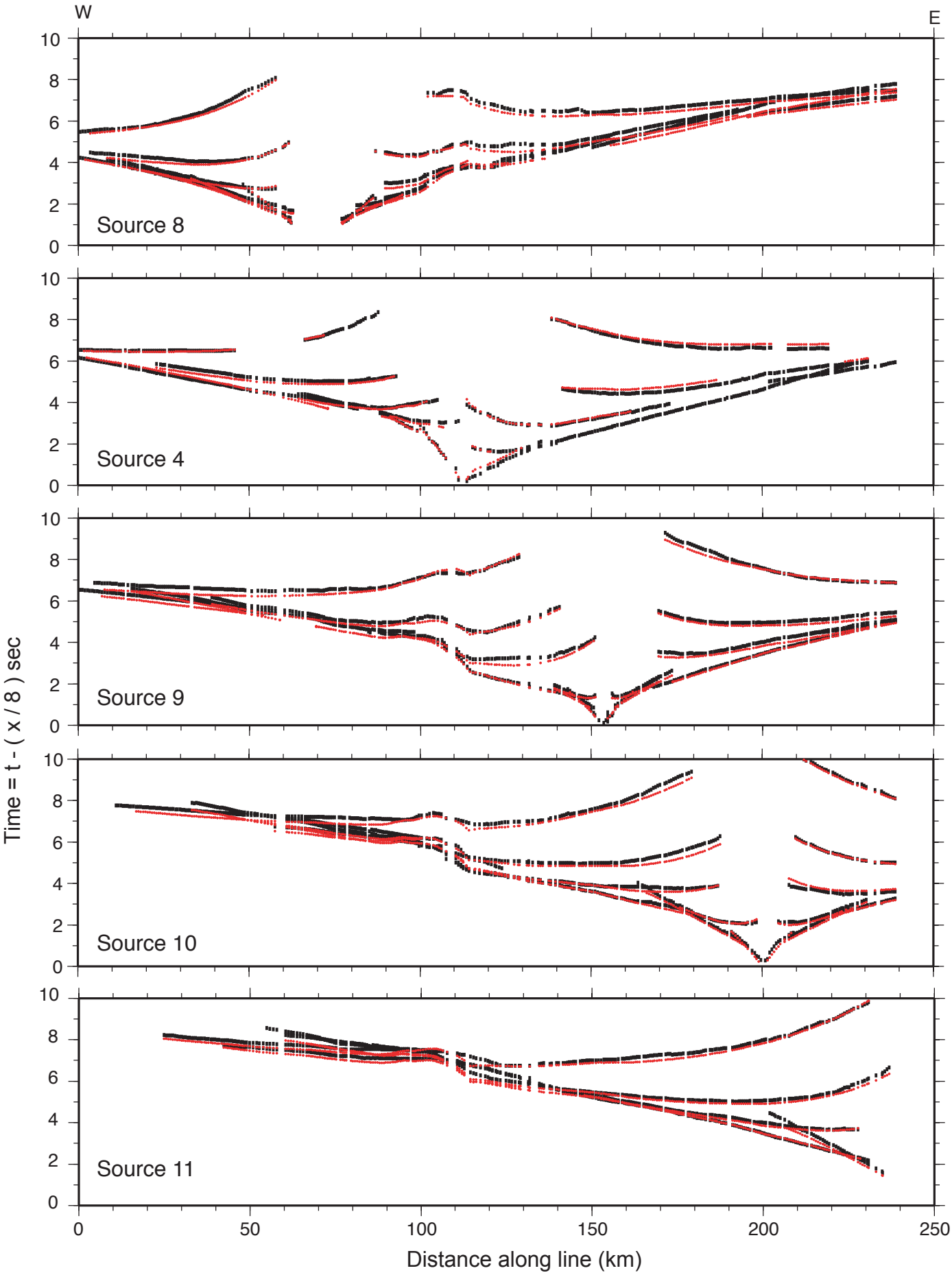
W
E
Source 8
Source 4
Source 9
Source 10
Source 11
Time = t - (x / 8) sec
Distance along line (km)
0
50
100
150
200
250
0
2
4
6
8
10

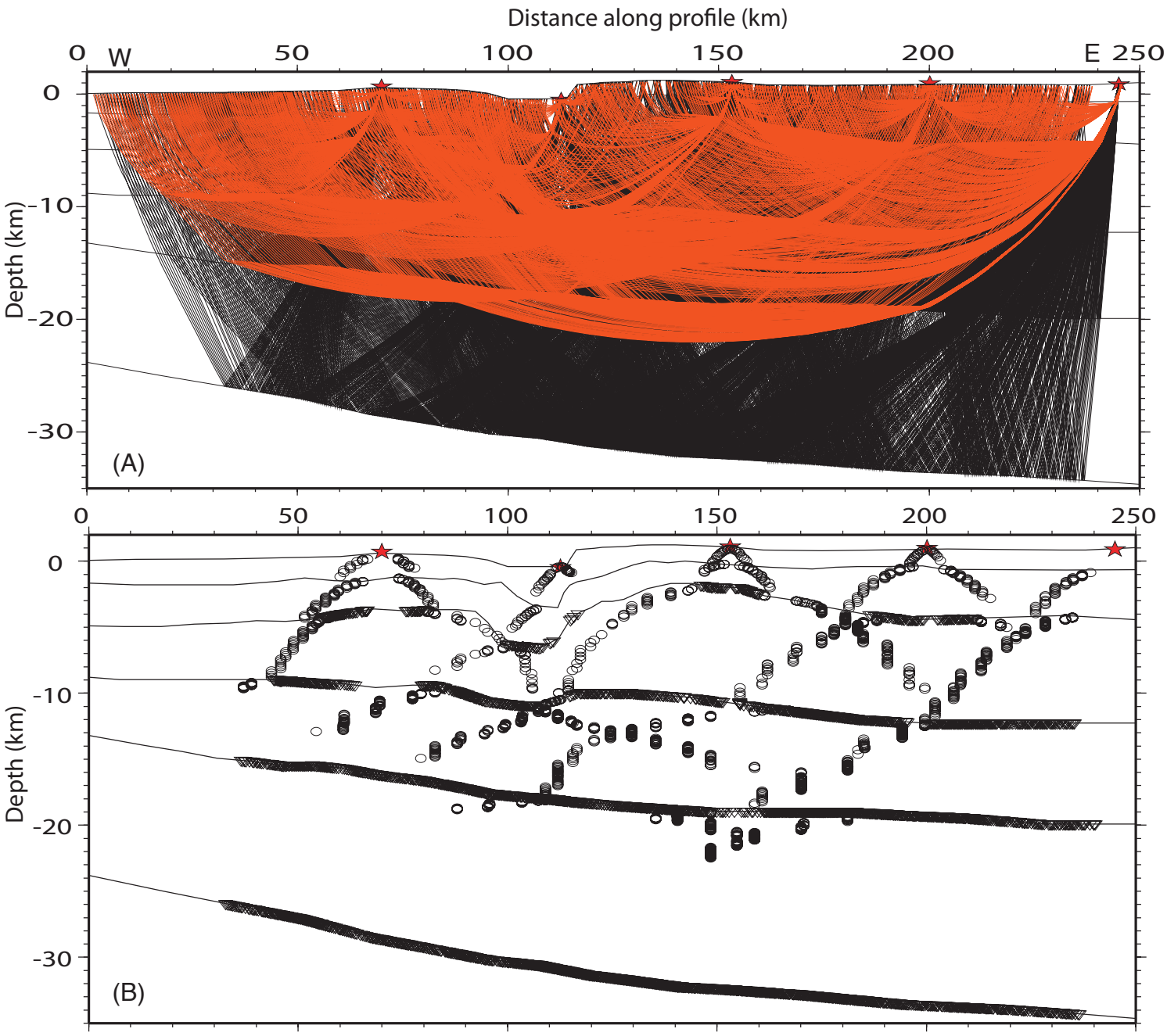
Distance along profile (km)
0
W
50
100
150
200
E
250
0
-10
-20
-30
Depth (km)
(A)
0
50
100
150
200
250
0
-10
-20
-30
Depth (km)
(B)

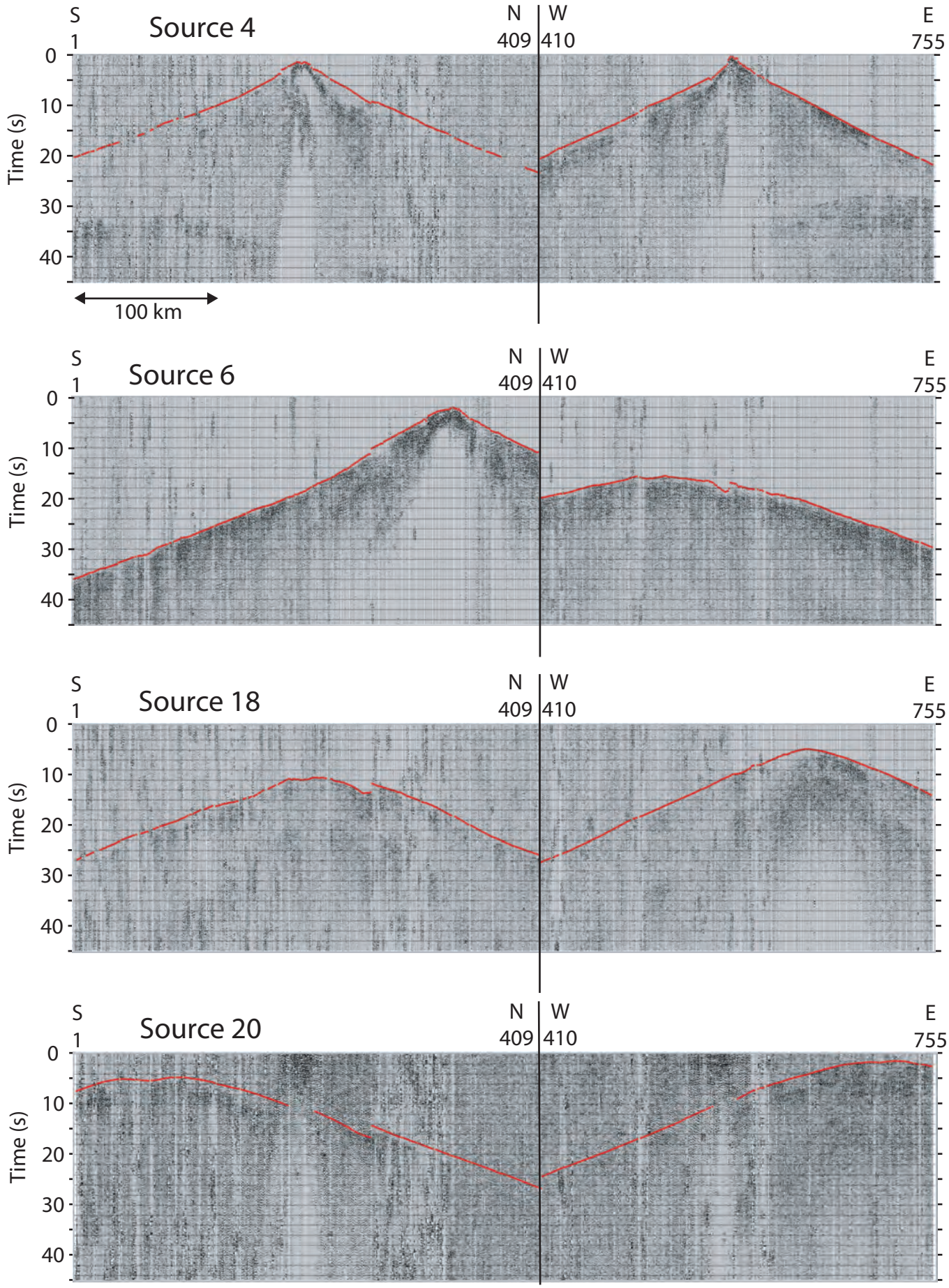
Source 4
S
1
N
409
W
410
E
755
Time (s)
0
10
20
30
40
100 km
Source 6
Source 18
Source 20

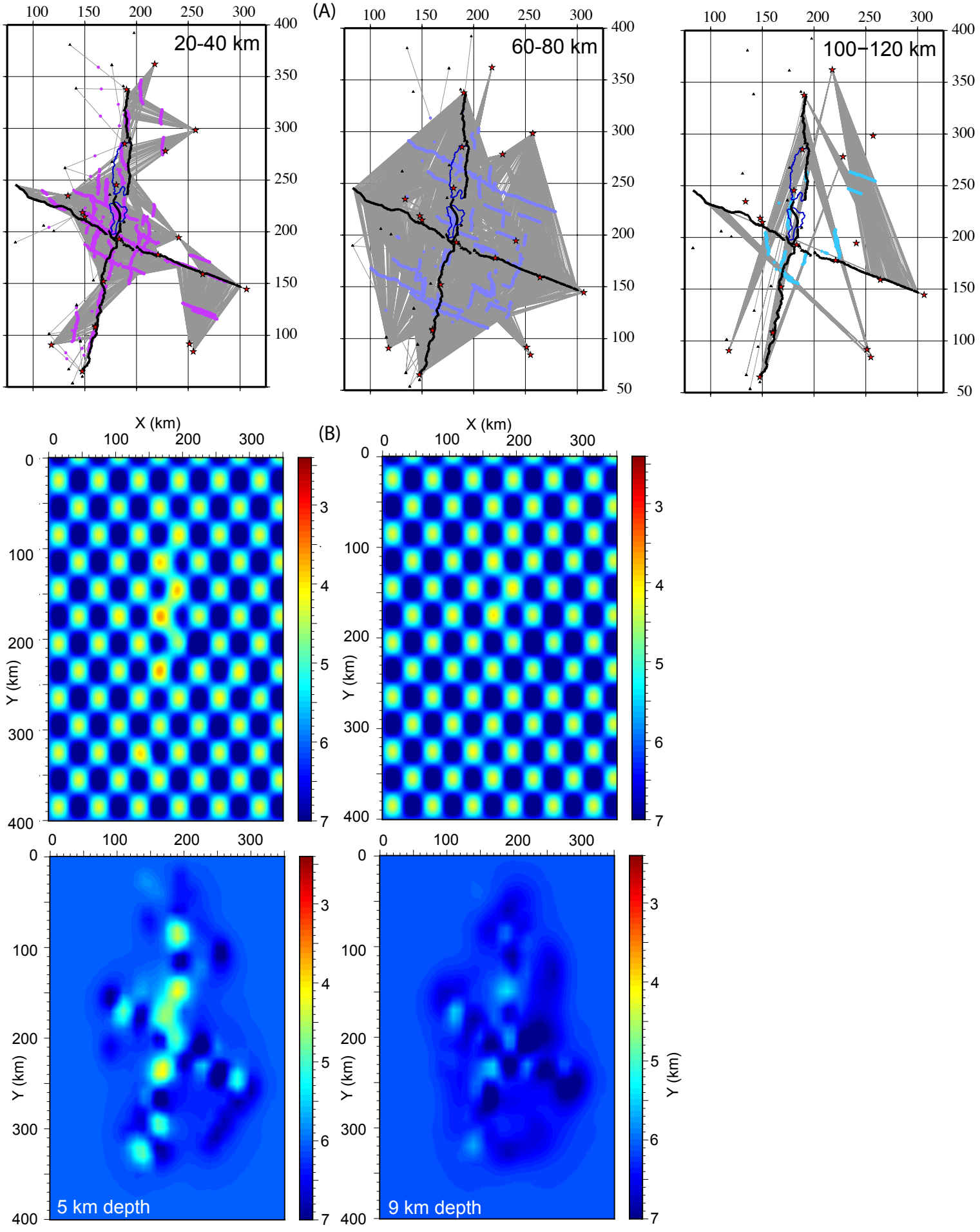
(A)
20-40 km
60-80 km
100−120 km
(B)
X (km)
Y (km)
5 km depth
9 km depth

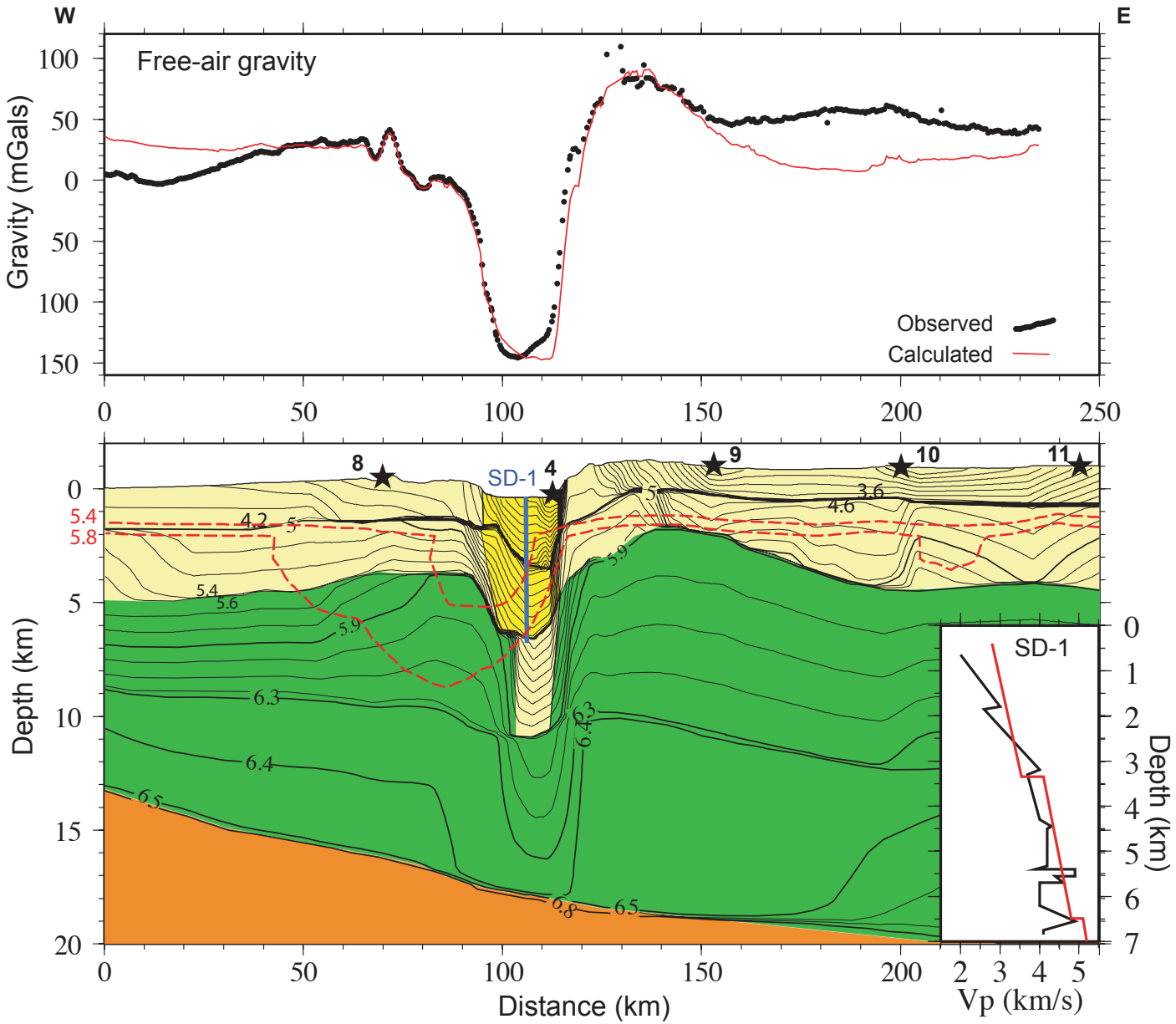
W
E
Free-air gravity
Gravity (mGals)
Observed
Calculated
8
SD-1
4
9
10
11
Depth (km)
Distance (km)
Vp (km/s)
SD-1
Depth (km)

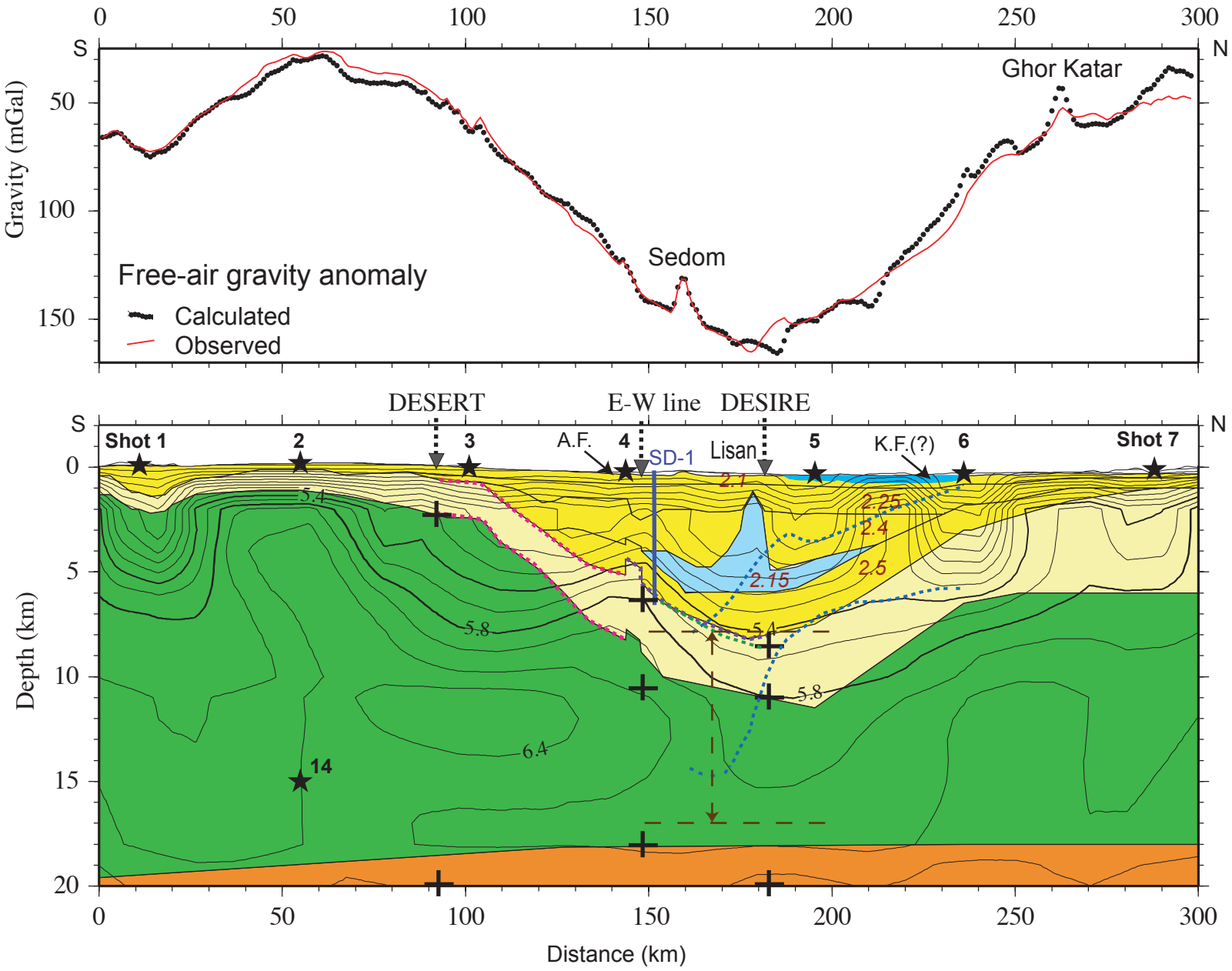
Gravity (mGal)
Free-air gravity anomaly
Calculated
Observed
Ghor Katar
Sedom
S
N
DESERT
E-W line
DESIRE
Shot 1
2
3
A.F.
4
SD-1
Lisan
5
K.F.(?)
6
Shot 7
14
5.4
5.8
6.4
2.1
2.25
2.4
2.5
2.15
Depth (km)
Distance (km)

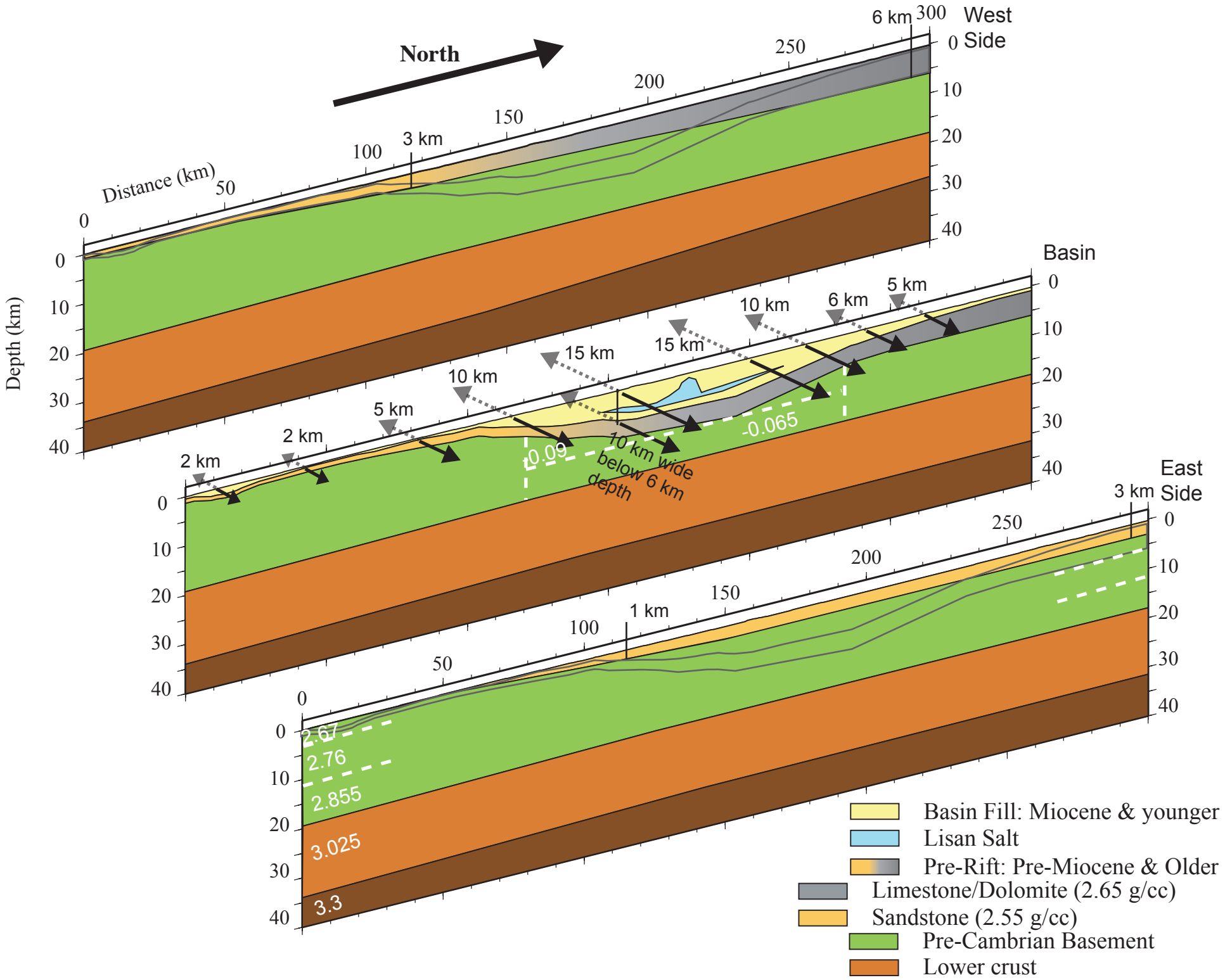
North
West Side
East Side
Basin
Distance (km)
Depth (km)
6 km
3 km
1 km
2 km
5 km
10 km
15 km
-0.09
-0.065
10 km wide below 6 km depth
2.67
2.76
2.855
3.025
3.3
Basin Fill: Miocene & younger
Lisan Salt
Pre-Rift: Pre-Miocene & Older
Limestone/Dolomite (2.65 g/cc)
Sandstone (2.55 g/cc)
Pre-Cambrian Basement
Lower crust

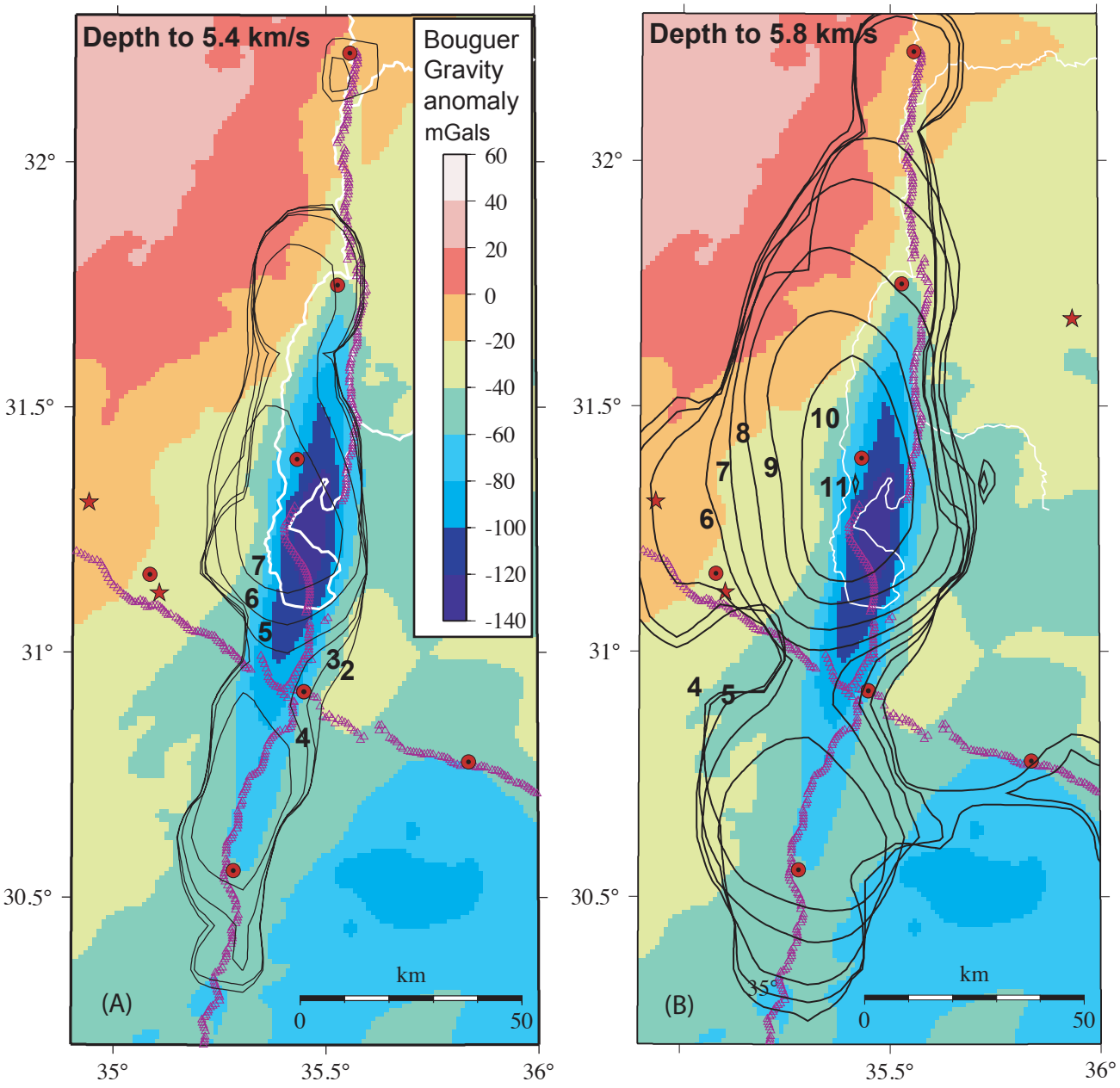
Depth to 5.4 km/s
Bouguer
Gravity
anomaly
mGals
60
40
20
0
-20
-40
-60
-80
-100
-120
-140
32°
31.5°
31°
30.5°
35°
35.5°
36°
7
6
5
3
2
4
km
0
50
(A)
Depth to 5.8 km/s
8
7
9
10
11
6
4
5
(B)

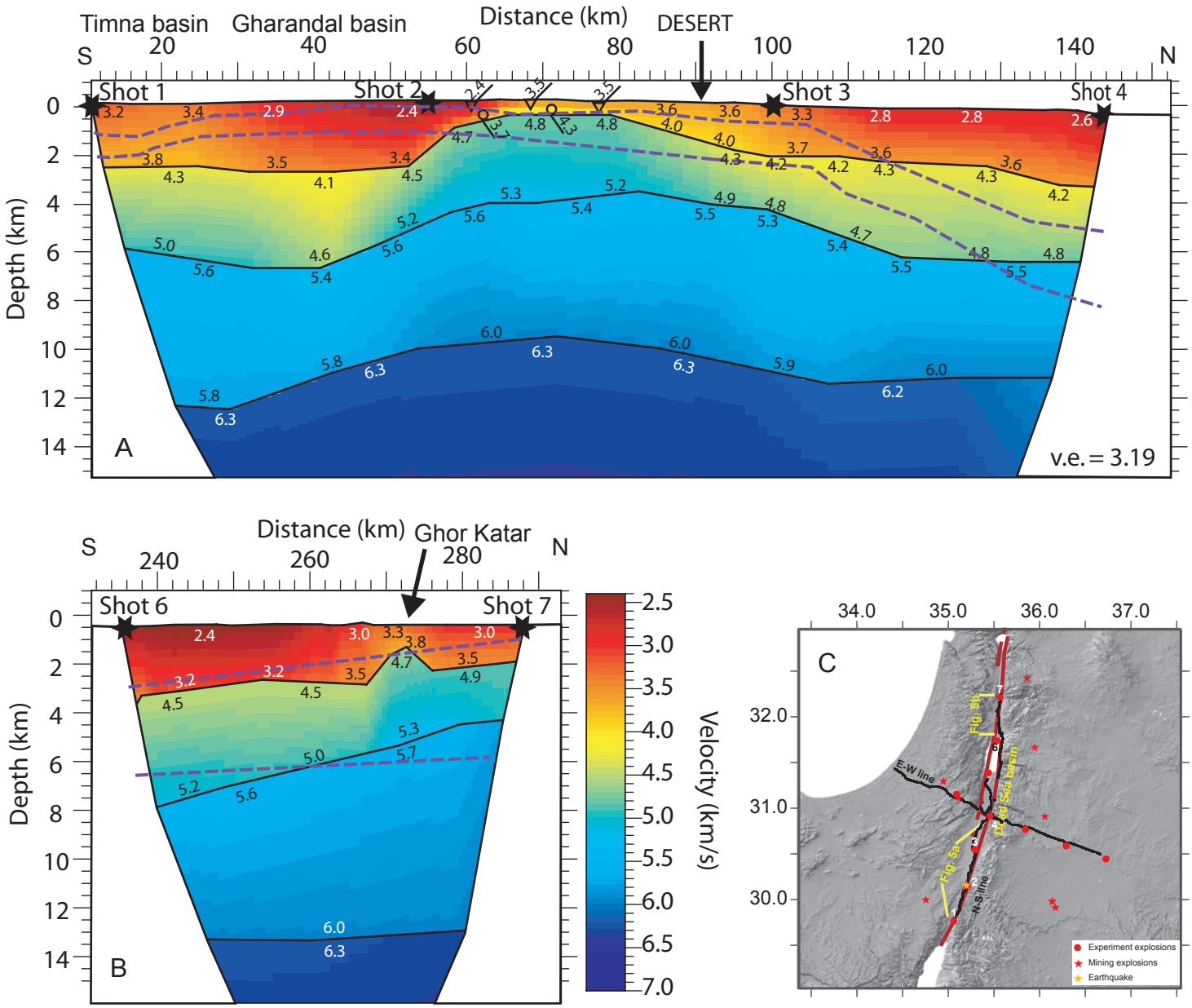
Timna basin
Gharandal basin
Distance (km)
DESERT
S
N
20
40
60
80
100
120
140
Shot 1
Shot 2
Shot 3
Shot 4
Depth (km)
0
2
4
6
8
10
12
14
A
v.e. = 3.19
Distance (km)
Ghor Katar
S
N
240
260
280
Shot 6
Shot 7
B
Velocity (km/s)
2.5
3.0
3.5
4.0
4.5
5.0
5.5
6.0
6.5
7.0
C
34.0
35.0
36.0
37.0
32.0
31.0
30.0
E-W line
N-S line
Fig. 5b
Fig. 5a
Dead Sea basin
Experiment explosions
Mining explosions
Earthquake

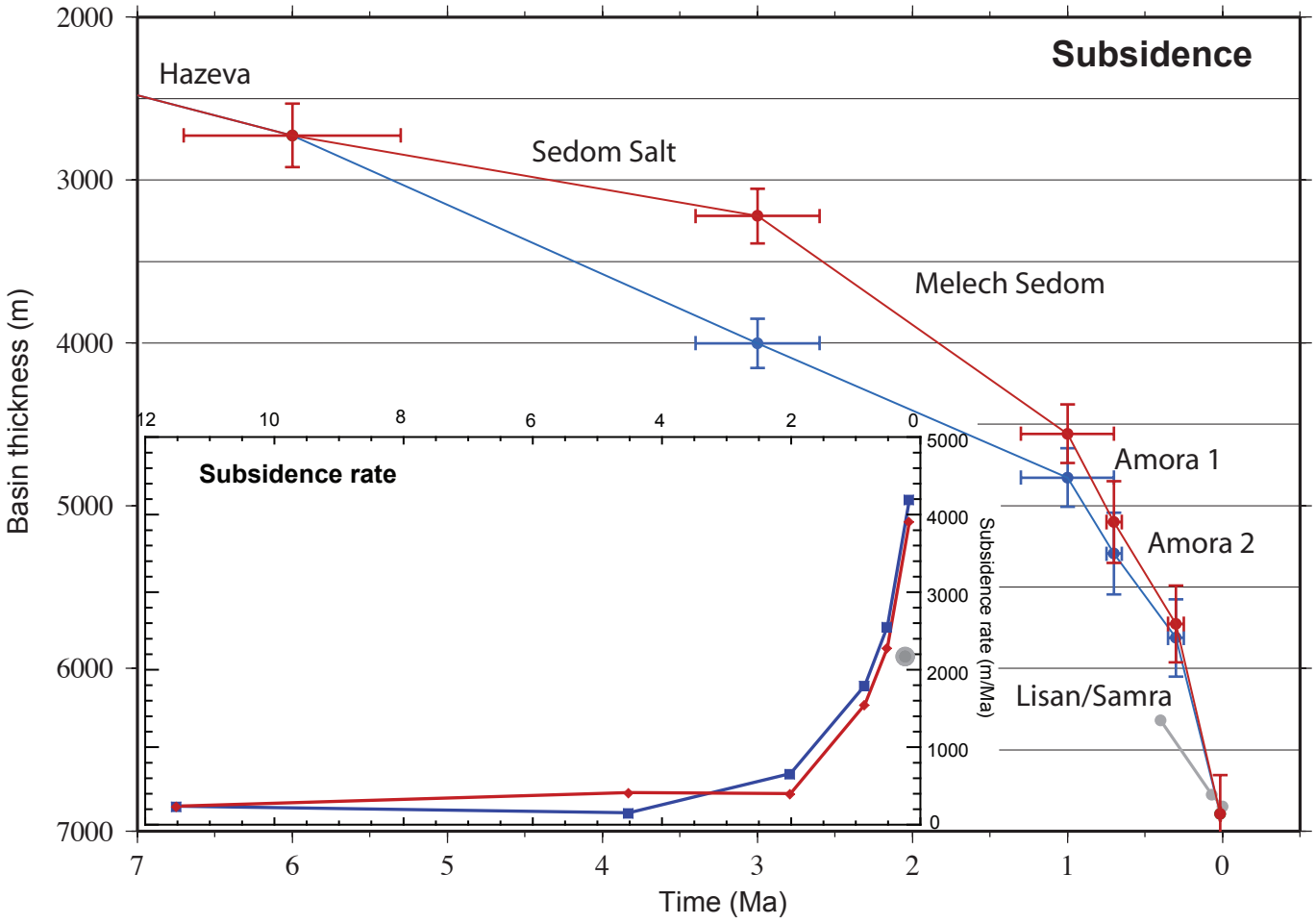
Subsidence
Hazeva
Sedom Salt
Melech Sedom
Amora 1
Amora 2
Lisan/Samra
Subsidence rate
Basin thickness (m)
Time (Ma)
Subsidence rate (m/Ma)
2000
3000
4000
5000
6000
7000
7
6
5
4
3
2
1
0
12
10
8
6
4
2
0
5000
4000
3000
2000
1000
0

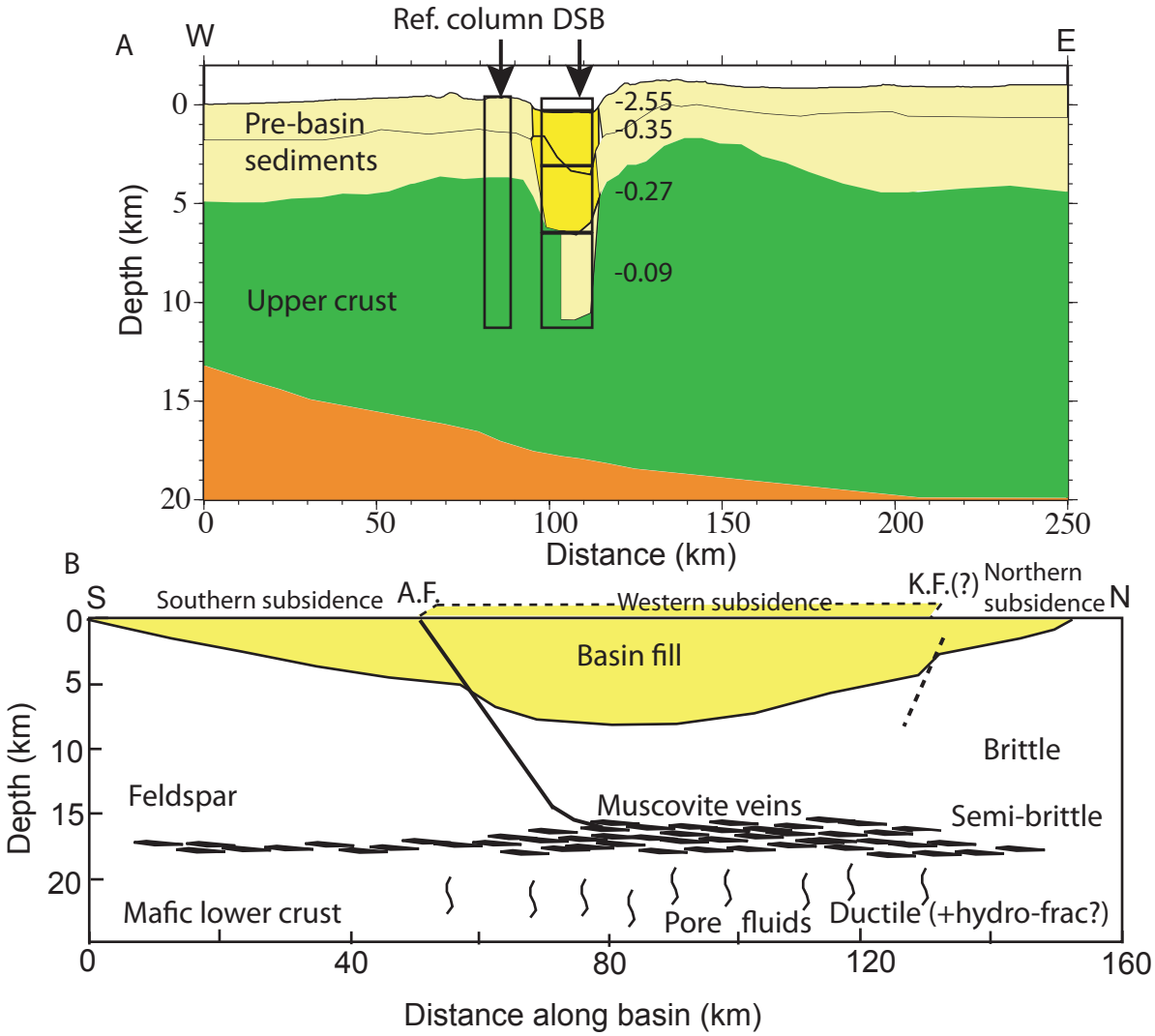
A
W
E
Ref. column DSB
Pre-basin
sediments
Upper crust
-2.55
-0.35
-0.27
-0.09
Depth (km)
0
5
10
15
20
0
50
100
150
200
250
Distance (km)
B
S
N
Southern subsidence
A.F.
Western subsidence
K.F.(?)
Northern
subsidence
Basin fill
Brittle
Feldspar
Muscovite veins
Semi-brittle
Mafic lower crust
Pore fluids
Ductile (+hydro-frac?)
Depth (km)
0
5
10
15
20
0
40
80
120
160
Distance along basin (km)

Table 1: Acoustic sources used in the tomographic inversion

Source	Type	Latitude	Longitude	Elevation (m)	# of phase picks	# of 1st arrivals
1	1000 kg explos.	29.7736	35.04994	63	208	592
2	1000 kg explos.	30.1572	35.18869	189	478	475
3	1000 kg explos.	30.5558	35.28107	13	462	575
4	1000 kg explos.	30.9210	35.44712	-305	1534	655
5	750 kg marine	31.3949	35.43104	-417.5	433	727
6	750 kg marine	31.7498	35.5270	-417.5	368	728
7	3000 kg explos.	32.2225	35.55687	-304.36	185	630
8	1000 kg explos.	31.1600	35.08220	515.69	1264	635
9	1000 kg explos.	30.7773	35.83613	1033	1162	654
10	1000 kg explos.	30.5973	36.2808	962	1127	415
11	1000 kg explos.	30.4536	36.71731	1008	1164	363
12	Mining explos.	31.6780	35.9377	650	n/a	299
13	Mining explos.	30.0092	34.7453	508	n/a	638
14	Earthquake	30.1675	35.1892	-15000	n/a	697
15	Mining explos.	31.1217	35.1050	555	n/a	633
16	Mining explos.	32.4375	35.8525	857	n/a	524
17	Mining explos.	29.9920	36.1287	895	n/a	724
18	Mining explos.	30.9210	36.0490	850	n/a	688
19	Mining explos.	31.8525	36.2517	640	n/a	377
20	Mining explos.	29.9250	36.1648	915	n/a	680
21	Mining explos.	29.9920	36.1287	895	n/a	693
22	Mining explos.	31.3062	34.9377	410	n/a	559

* Marine – marine explosion suspended ~50 m below the lake surface. Explos. - explosion

Table 2: Details of the iteration procedure in the tomographic inversion

Tomography		
Iteration # (Cell size)	**RMS (ms)**	**Chi ^2**
Starting Model	997.46185	14.8720
Iteration 1 (25x25x5 km)	830.54474	10.2739
Iteration 2 (20x20x5 km)	772.82867	8.8199
Iteration 3 (10x10x1 km)	736.02740	7.9627
Iteration 4 (10x10x1 km)	631.39069	5.8002
Iteration 5 (10x10x1 km)	546.15936	4.3257
Iteration 5 (10x10x1 km)	521.26697	3.9322
Wide Angle	**RMS (ms)**	**Chi ^2**
East-West Profile	145.0	2.097
North-South Profile	469.0	22.042
Gravity	**Error (mGal)**	
East-West Profile	22.255*	
North-South Profile	4.22	

*Model is solely based on conversion of *P* wave velocity structure to density structure

Table 3: Parameters used to correct for sediment porosity

Lithology	**Phi value**	**C (1/km)**
Sand	0.490	0.270
Quartz Sand	0.620	0.360
Shale-Sand	0.560	0.390
Shale-Clay	0.630	0.510
Carbonate/Calcite	0.240	0.540
*Marl	0.435	0.525
*Sand-Marl	0.4918	0.3953

Notes:

*Marl = 50% Shale-Clay + 50% Carbonate/Calcite

*Sand-Marl = 50% Sand + 32.5% Shale-Clay + 17.5% Carbonate/Calcite